A FAST PLASMA TOMOGRAPHY ROUTINE WITH SECOND-
ORDER ACCURACY AND COMPENSATION FOR SPATIAL
RESOLUTION

P. Smeulders

IPP 2/252   July 1983

IPP

MAX-PLANCK-INSTITUT FÜR PLASMAPHYSIK

8046 GARCHING BEI MÜNCHEN

MAX-PLANCK-INSTITUT FÜR PLASMAPHYSIK

GARCHING BEI MÜNCHEN

A FAST PLASMA TOMOGRAPHY ROUTINE WITH SECOND-
ORDER ACCURACY AND COMPENSATION FOR SPATIAL
RESOLUTION

P. Smeulders

IPP 2/252   P. Smeulders   A FAST PLASMA TOMOGRAPHY ROUTINE
WITH SECOND-ORDER ACCURACY AND
COMPENSATION FOR SPATIAL
RESOLUTION

Abstract

If the rotation of the mode structures in front of an
X-ray pinhole camera is known, the full cross-section of the
structures can be obtained. Where various modes are observed
simultaneously, the experimental well-established phase
coupling of these modes is implied. This allows the transi-
tion from time to poloidal angle to be made and modes with
different toroidal mode numbers to be separated. With one
pinhole camera, however, it is not possible to separate more
than two modes with different poloidal mode numbers. In the
first sections the computer code is described; examples of
various tearing modes measured in a current-carrying stella-
rator plasma are then presented. The time evolution and the
structure of these modes is discussed.

- 1 -

Contents

Introduction

Tomography methods have found widespread application in
several areas of research. The various methods and their
applications are reviewed in Refs. /1/ and /2/.

Tomography methods in nuclear fusion research are also based
on Fourier reconstruction /3/ and /4/, iterative methods /5/
and filtered back projection /6/ in order to reconstruct
radiation-emitting structures in the plasma cross-section.
Filtered back projection is essentially identical to
Fourier reconstruction, and so tomography routines can be
divided into two groups:
1. Fourier space reconstruction
2. Real space reconstruction.
Other ways of obtaining the emitting structure of the
plasma cross-section, which are employed in Refs. /7/ and
/8/, are effectively a "human" iteration routine. This is
mostly a time-consuming process, but in certain cases a ne-
cessary one, especially where problems are ill-posed: the
number of knowns (projections) is less than the number of
unknowns (grid points). The uniqueness of solutions usually
remains a problem with tomography methods. Fourier reconstruc-
tion reduces the number of solutions by filtering in the
k-Fourier space. Real space reconstruction reduces the number
of solutions by some kind of least squares fit smoothing
method.

X-ray emission cross-sections in fusion research plasmas
usually have a steep radial dependence. This requires a
high k radial wave number when using a Fourier space re-
construction scheme with a linear interpolation method.
Filtering methods in Fourier reconstruction tend to limit
the k-wave number,thus conflicting with the requirements for
steep gradients.

Real space reconstruction in conjunction with a second-order
accurate interpolation scheme /9/ allows steep gradients in

the X-ray emission. This method also permits ready compensation for the spatial resolution. The second-order interpolation scheme further allows the number of unknown grid points to be reduced. By putting this number equal to the number of measured "line" integrals (projections) the problem becomes a well-posed one with a "unique" solution, especially in the case of bell-shaped radial profiles. An iteration process is therefore no longer required in principle.

1. Choice of Tomography Method

Fourier and real space reconstruction techniques probably show little difference in the resulting image when using appropriate interpolation and smoothing or filtering routines.

By limiting the bandwidth or the k-wave numbers smoothing is obtained in the case of the Fourier technique. Interpolation is needed to make the required transition from an equal spacing in radius to an equal spacing in k-space. A correction for the spatial resolution can be made by a convolution technique /10/. When using a linear interpolation scheme in Fourier or real space reconstruction about twice the number of grid points are necessary in order to obtain the same accuracy for typical cylindrically symmetric X-ray emission cross-sections as compared with second-order inversion techniques /9/.

It is obviously of advantage to use a second-order interpolation method in X-ray flux measurements in fusion research

experiments. The real space reconstruction technique des-
cribed here uses such an interpolation scheme. The same
sort of scheme was also used in Ref. /9/ in order to cal-
culate the influence of the spatial resolution. In this
report, however, the influence of the spatial resolution
on the flux signals (projections) and the inversions
(reconstruction) is calculated differently. It is possible
to express the real projections as linear functions of
projections that possess ideal spatial resolution. By
simple matrix inversions the ideal spatially resolved pro-
jections are obtainable from the real projections (band
matrix inversion).

By making the number of grid points equal to the total
number of projections, not only can unique solutions be
obtained, especially for bell-shaped radial cross-sections,
but also just relatively smooth functions are allowed. The
latter is based on the second-order interpolation method,
which only allows parabolic functions to exist in between
grid points. This is equivalent to the bandwidth limitation
in the Fourier reconstruction schemes. Because real space
reconstruction is an analogon of cylindrically symmetric
Abel inversion, it is in principle stripping reconstruction:
the local intensity is given by the projection through that
point minus the projection through an outer neighbouring
grid point.

2. Plasma X-ray Diagnostics and Stripping Reconstruction

The set-up of the real space reconstruction method must be
closely related to the experimental set-up of the X-ray
diagnostic and to the behaviour of the modes that are
present in the plasma.

In the Wendelstein VII-A stellarator /11/ a fixed
array of 30 detectors in a fan beam geometry is used
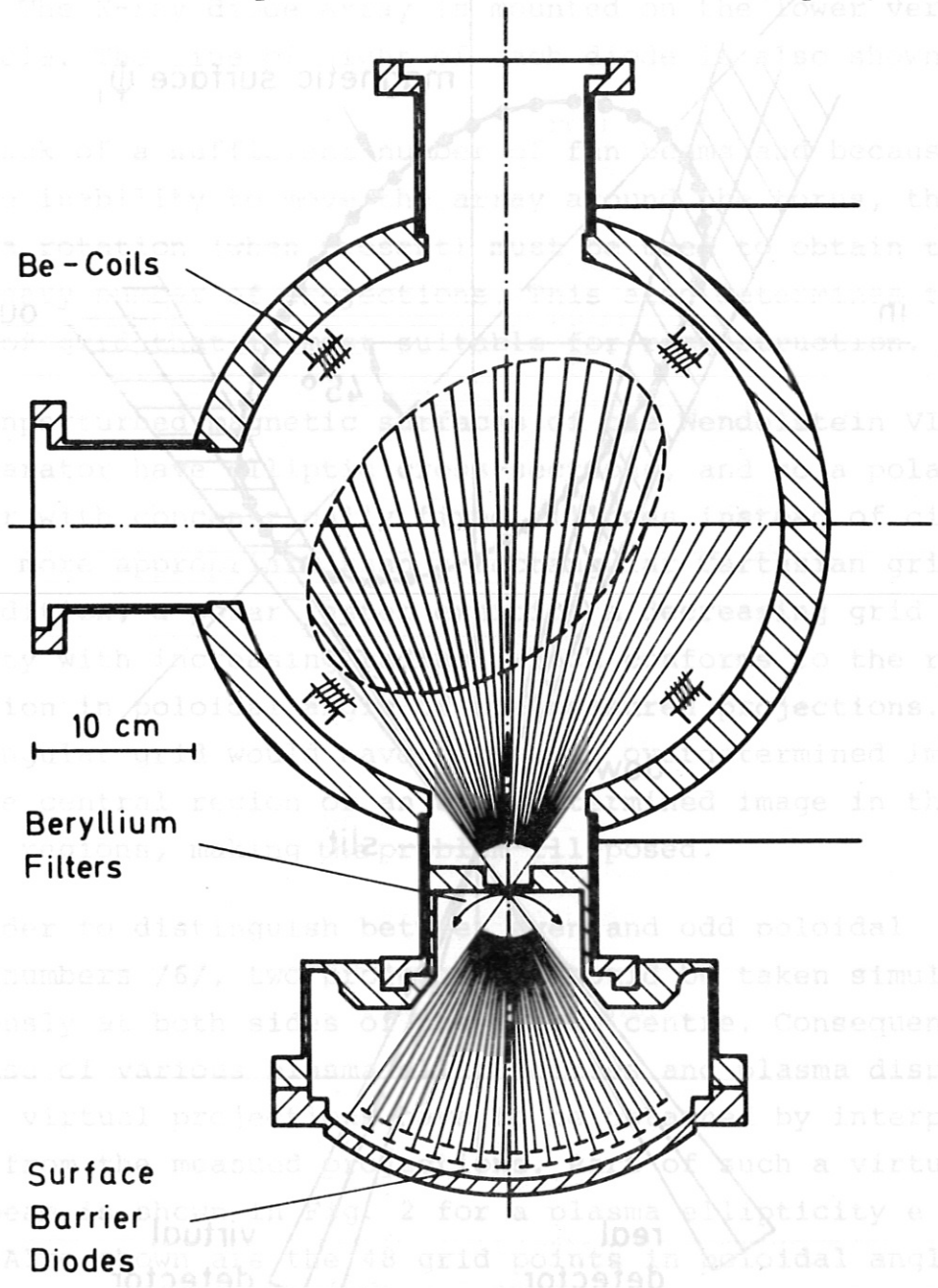to measure the X-ray emission of a slice of the plasma.
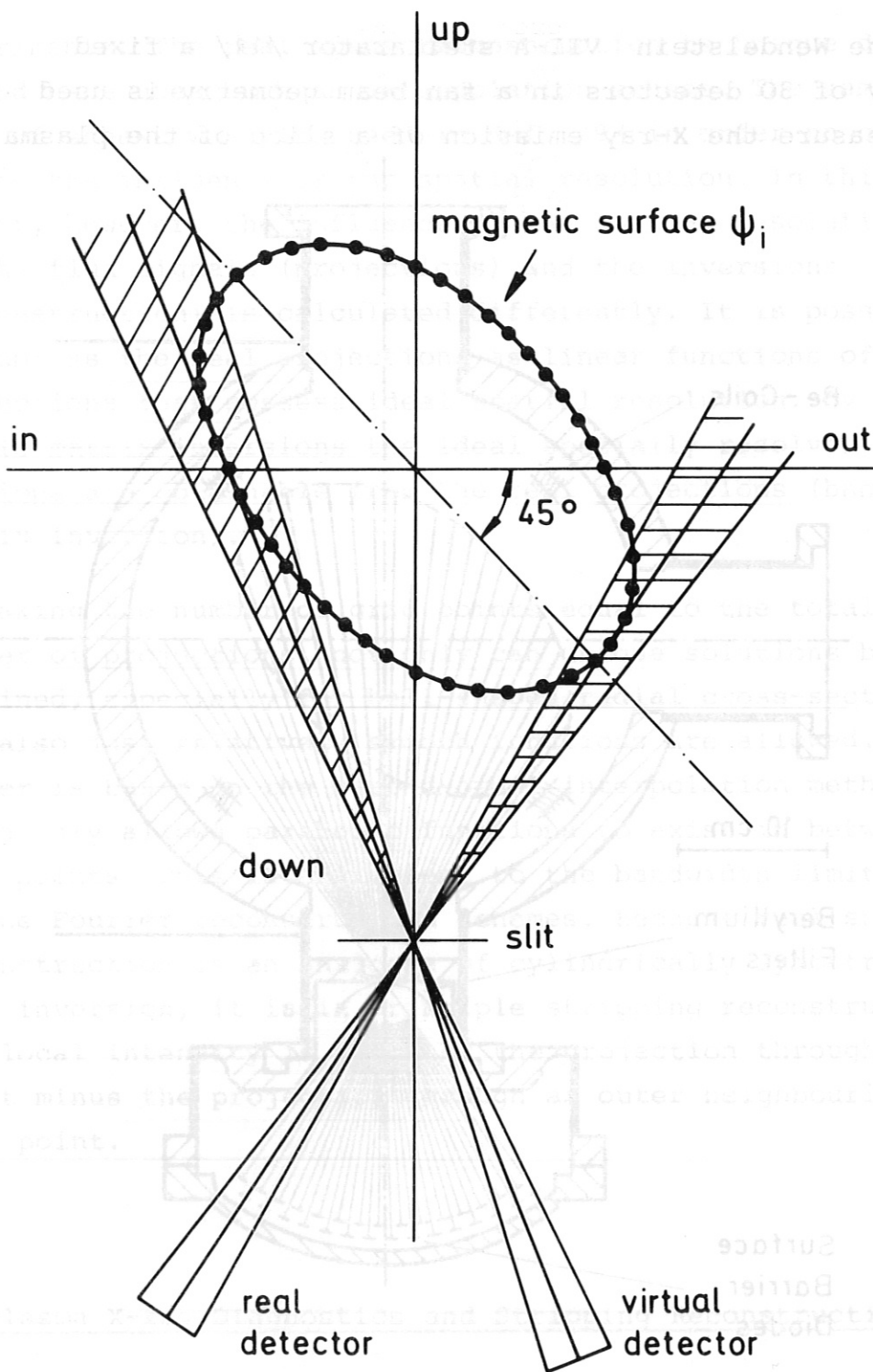

Fig. 1 The ultra soft X-ray pinhole camera

IPP3- SME 417-83

Fig. 2

IPP3- SM E 418-83

Figure 1 shows a cross-section of the toroidal vacuum vessel with the elliptically shaped stellarator plasma inside. The X-ray diode array is mounted on the lower vertical porthole. The line of sight of each diode is also shown.

For lack of a sufficient number of fan beams and because of the inability to move the array around the torus, the plasma rotation (when present) must be used to obtain the necessary number of projections. This also determines the kind of grid that is most suitable for reconstruction.

The unperturbed magnetic surfaces of the Wendelstein VII-A stellarator have elliptic cross-sections, and so a polar raster with concentrically fixed ellipses instead of circles seems more appropriate than a rectangular Cartesian grid. In addition, a polar raster exhibits a decreasing grid density with increasing radius, which conforms to the resolution in poloidal angle of the measured projections. A rectangular grid would have either an overdetermined image in the central region or an underdetermined image in the outer regions, making the problem ill-posed.

In order to distinguish between even and odd poloidal mode numbers /6/, two projections should be taken simultaneously at both sides of the plasma centre. Consequently, because of various plasma ellipticities and plasma displacements virtual projections have to be obtained by interpolation from the measued projections. Part of such a virtual fan beam is shown in Fig. 2 for a plasma ellipticity e of 2/3. Also shown are the 48 grid points in poloidal angle on each elliptical surface. This number should be sufficient to resolve the observed poloidal mode structures.

The modes are observed either clearly separated in space
and time or in pairs phase coupled or mode locked /11/.
This latter coupling occurs especially at large
mode amplitudes. The phenomenon is included in the recon-
struction, which allocates a time period T to various
poloidal angles, depending on the observed mode number:
The same time period T is allocated to 360° for an m = 1
and to 180° for a m = 2 mode.

3. Flux or Projection Calculation

Each projection is calculated along its line of sight.
This line is defined by the position of the slit of the
fan beam at (X_o, Y_o) and the point (X_i, Y_i) of the
ellipses of mean radius r_i with which the line is tangent
(Fig. 3). The ellipses are orientated at an angle
$\theta_o = -45^\circ$ with respect to the horizontal axis of the
toroidal vacuum vessel.

The line integral is obtained by integrating over each
segment marked by the crossing-points of the line of sight
and the various elliptic magnetic surfaces with $r_j > r_i$.
The ellipses are defined by

$$e^2 x^2 + y^2 = \Psi_i = \frac{e^2+1}{2} r_i^2 , \tag{1}$$

where $e = b/a$ is the ratio of the minor (b) over the major
(a) axis of the ellipse. Each elliptic magnetic surface is
defined by its value Ψ_i or by its mean radius r_i.

The lines l_i tangential to an ellipse Ψ_i are given by the
following equations:

$$Y - Y_o = m_i (x-x_o) \text{ with}$$

$$m_{i1,2} = tg \; \alpha_{i1,2} = \frac{e^2 X_o Y_o \pm e^2 \sqrt{\Psi_i (Y_o - \Psi_i)}}{e^2 X_o^2 - \Psi_i} \tag{2}$$
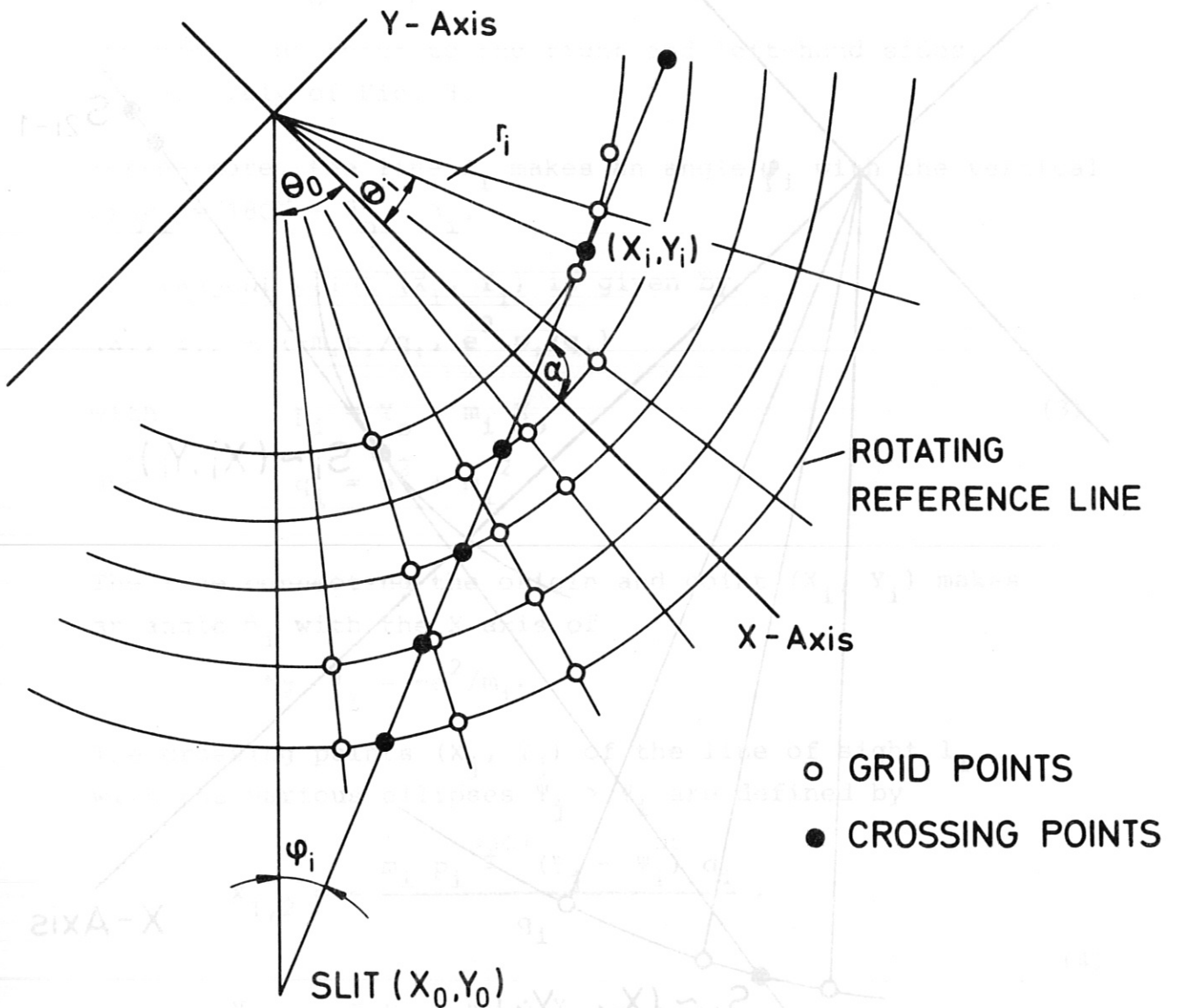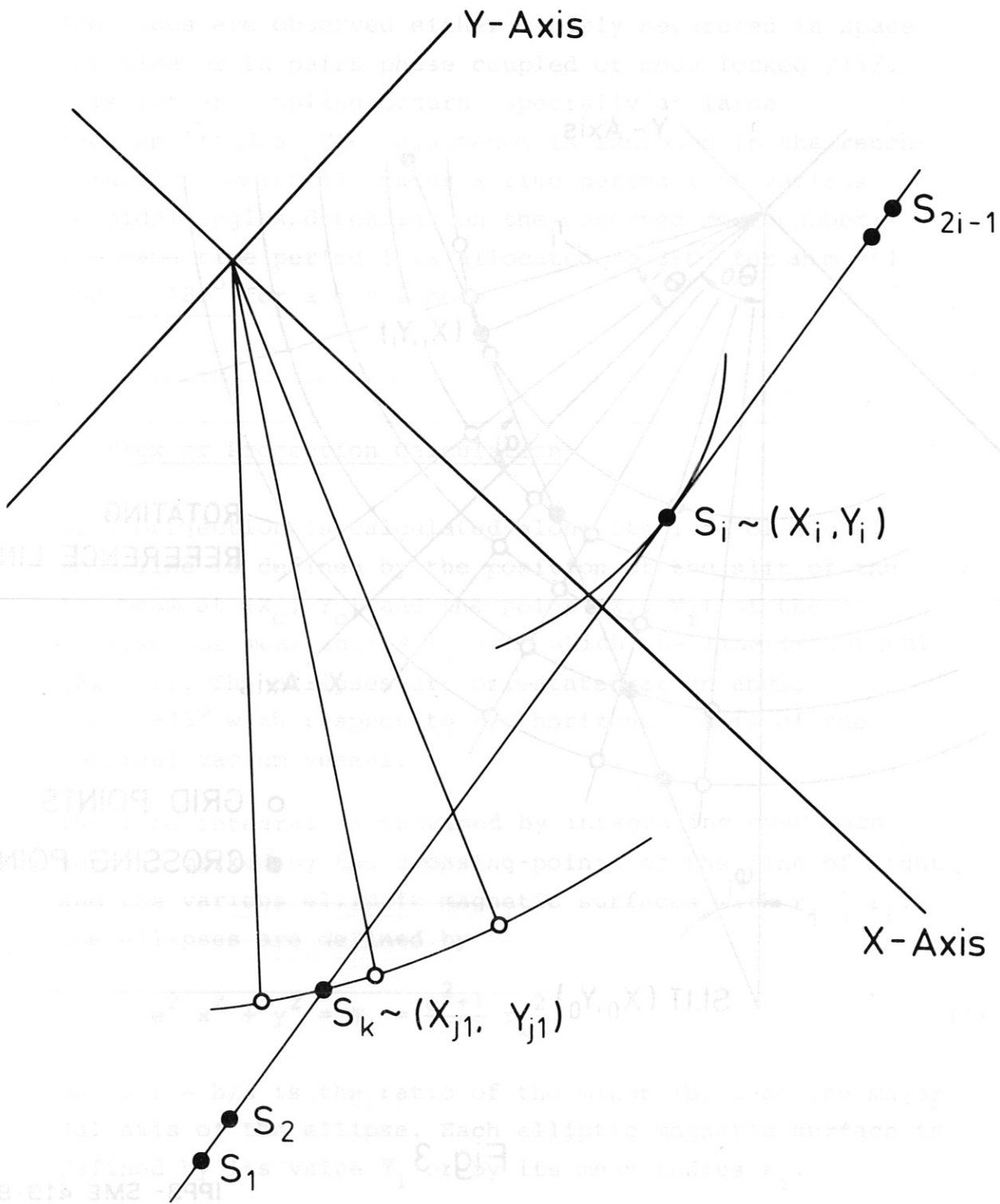
Fig. 3

IPP3- SME 419-83

Fig. 4

and $\Psi_o = e^2 X_o^2 + Y_o^2$

The -/+ signs refer to the right and left-hand sides, respectively of Fig. 3.

Furthermore, the line l_i makes an angle φ_i with the vertical of $\varphi_i = 180^o + \theta_o - \alpha_i$.

The tangent point (X_i, Y_i) is given by

$(X_i, Y_i) = (-m_i p_i/q_i, \ e^2 p_i/q_i)$

with $\qquad\qquad p_i = Y_o - m_i X_o$ $\qquad\qquad\qquad\qquad$ (3)

and $\qquad\qquad q_i = e^2 + m_i^2$

The line connecting the origin and point (X_i, Y_i) makes an angle θ_i with the X axis of

$$tg \ \theta_i = -e^2/m_i.$$

The crossing points (X_j, Y_j) of the line of sight l_i with the various ellipses $\Psi_j > \Psi_i$ are defined by

$$X_{1,2} = -\frac{m_i p_i \pm (\Psi_j - \Psi_i) q_i}{q_i},$$

$$(4)$$

$$Y_{j \ 1,2} = p_i + m_i \cdot X_{j \ 1,2}.$$

The -/+ signs are connected to crossing points on the same ellipse respectively above and below the tangent point (X_i, Y_i).

The various angles that the lines connecting the origin to the crossing-points (X_j, Y_j) make is then given by
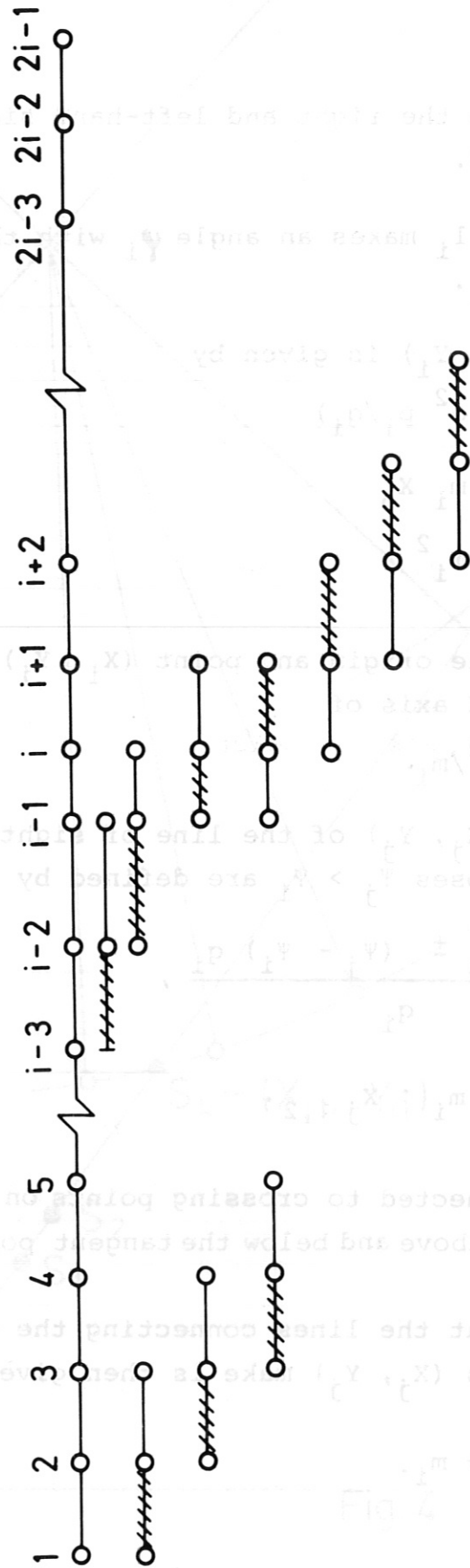
$$tg \ \theta_j = \frac{p_i}{X_j} + m_i. \qquad\qquad (5)$$

Fig. 5

IPP3-SME 421-83

The length of the line of sight taken from its crossing-point with the X axis is given (Fig. 4) by

$$S = X \sqrt{m_i^2 + 1}. \tag{6}$$

The line integral can now be written as

$$\Phi_i = \int_{S1}^{S_{2i-1}} f \, ds = \sum_{k=1}^{2i-1} a(k,i) \, f_k^c. \tag{7}$$

The value of the intensity at the crossing-point f_k^c can be written as a sum of the values of poloidally neighbouring grid points:

$$f_k^c = \sum_{l=m}^{m+2} b_l \, f_{kl}. \tag{8}$$

The constants b_l are obtained from the second-order interpolation scheme, applied in the poloidal direction (along the elliptic magnetic surface):

$$\begin{aligned}
b_m &= (u-1)(u-2)/2, \\
b_{m+1} &= -u(u-2), \\
b_{m+2} &= u(u-1)/2,
\end{aligned} \tag{9}$$

with $u = \theta_k/\Delta\theta - \text{Int}\,(\theta_k/\Delta\theta)$.

$\Delta\theta$ is the step size in θ, in our case usually 15°. The function Int yields the integer part of the variable X. The angle θ_k is obtained from eq. (5) by replacing j by k and taking $X_k = X_{j1}$ for $k \leq i$ and $X_k = X_{j2}$ for $k > i$.

The constants $a(k,i)$ of eq. (7) are obtained as indicated schematically in Fig. 5. Each segment contributes several times to a particular $a(k,i)$ belonging to crossing-point k. The integral over segment k can be written as:

$$\int_{S_k}^{S_{k+1}} f \, ds = d(1,k) f_n + d(2,k) f_{n+1} + d(3,k) f_{n+2},$$ (10)

where n can be either k or k-1 and

$$d(1,k) = \frac{((ds/3 - (C_2 + C_3)/2) \cdot ds + C_2 \cdot C_3) \cdot ds}{(S_n - S_{n+1}) \cdot (S_n - S_{n+2})},$$

$$d(2,k) = \frac{((ds/3 - (C_3 + C_1)/2) \cdot ds + C_3 \cdot C_1) \cdot ds}{(S_{n+1} - S_{n+2}) \cdot (S_{n+1} - S_n)},$$

$$d(3,k) = \frac{((ds/3 - (C_1 + C_2)/2) \cdot ds + C_1 \cdot C_2) \cdot ds}{(S_{n+2} - S_n) \cdot (S_{n+2} - S_{n+1})},$$

with $C_1 = S_n - S_k$, $C_2 = S_{n+1} - S_k$, $C_3 = S_{n+2} - S_k$, and

$$ds = S_{k+1} - S_k.$$

This results in the following relations for $a(k,i)$ (see Fig. 5):

$$a(1,i) = d(1,1),$$
$$a(2,i) = d(2,1) + d(1,2),$$

for $2 < k < i-1$,

$$a(k,i) = d(3,k-2) + d(2,k-1) + d(1,k),$$ (11)
$$a(i-1,i) = d(3,i-3) + d(2,i-2) + d(1,i-1) + d(1,i),$$
$$a(i,i) = d(3,i-2) + d(2,i-1) + d(2,i) + d(1,i+1),$$
$$a(i+1,i) = d(3,i-1) + d(3,i) + d(2,i+1) + d(1,i+2),$$

for $i+1 < k < 2i-2$,

$$a(k,i) = d(3,k-1) + d(2,k) + d(1,k+1),$$

$$a(2i-2,i) = d(3,2i-3) + d(2,2i-2),$$
$$a(2i-1,i) = d(3,2i-2).$$

It should be noted that the terms a(k,i) are symmetric round k=i: a(k,i) = a(2i-k,i). Third and fourth-order interpolation schemes were also tested in the line integration. Oscillations in the end product appeared, however, in the case of steep radial profiles.

Using higher-order interpolation schemes apparently has similarities with too large bandwidths in Fourier space reconstruction.

4. Real Space Reconstruction

In essence there is no difference between simulating the measurements, i.e. calculating the line integrals for various times from an assumed model, and reconstructing the mode structure in the plasma from the measured signals.

The line integration method expressed in eqs. (7) and (8) is also the basis for real space reconstruction. The flux can be written as

$$\Phi_i = \sum_{k \neq i} a(k,i) \sum_{l=m}^{m+2} b_l f_{kl} + a(i,i) f_i^c \tag{12}$$

this being the sum of known local emissivities and the one unknown, viz. f_i^c; k,i are radial indices and m,l are poloidal indices. The reconstruction starts at the plasma edge, which, by definition, has zero emissivity. The position of the plasma edge at r=a is determined by the program through extrapolation of the outer signals. The value of "a", that is usually found in this way, is close to the vacuum vessel wall and not to the plasma limiter.

As in the Abel inversion method, the procedure in eq. (12) is repeated until the plasma centre is reached. The known terms f_{kl} contain the contribution of the various modes present at that particular magnetic surface. The contribution of each mode to the time-dependent signal Φ_i is given by the phase coupling mechanism described in Ref. /11/. This mechanism can be explained by the potential magnetic energy well, that exists between two helical current channels in a torus /13/. This well couples the two current channels together as if a pure radial uniform toroidal rotation were taking place. In this case the frequency of each mode is determined by its toroidal mode number n:

$$f = f(\omega t + m^+ \varphi)$$

with
$$\omega = n\, v/r.$$
(13)

v is the apparent poloidal velocity in front of the camera, r is the radial position of the magnetic surface, $m^+ = m/n$, where m,n are the poloidal and toroidal mode number respectively, and φ is the poloidal phase angle in real space.

Furthermore, the modes are assumed to rotate along the magnetic surfaces, which in the case of the Wendelstein VII-A stellarator are concentric ellipses inclined at 45° to the horizontal axis, as shown in Fig. 1. By subtracting the contribution of the outer magnetic surfaces

$$\sum_{k \neq i} a(k,i) \sum_{l=m}^{m+2} b_l\, f_{kl}$$

from Φ_i and dividing by $a(i,i)$ one obtains the contribution of crossing-point i: f_i^c as a function of time $\theta = \omega t$. The separation of the various modes from these two time-varying quantities at the right and left of the plasma centre is shown next.

5. Separation of Modes with Different Toroidal Mode Numbers

The value of the toroidal mode numbers n can only be determined with a second pinhole camera. This camera also increases the resolution power for the poloidal mode numbers of the various modes that can be present in the plasma.

A truly unique solution is theoretically never really possible with fixed pinhole cameras because various combinations of modes can lead to identical signals. This is shown in one of the following sections. In practice, however, more than one camera will reduce the number of physically possible modes to an acceptable level. In the case of the Wendelstein VII-A experiment only two detectors ±2.3 cm off the plasma centre were available to function as a second camera. This is insufficient in most cases, and only with information from magnetic pick-up or mirror coils distributed poloidally and toroidally around the torus has it been possible to determine the various modes unambiguously.

It was found that when the mode amplitudes become sufficiently large mode coupling occurs and modes with identical toroidal mode numbers have an identical periodicity in time. Higher harmonics in this periodicity are therefore linked to higher toroidal mode numbers.

Mode coupling has been explicitly incorporated in the computer code.

If no mode coupling occurs at small mode amplitudes, the modes appear to be localized in space. This makes it possible to analyze each mode separately.

By allocating a particular interval of time t of the measured signals to a time period T a particular toroidal mode number is selected. For example, the choice of one period in the period T selects all values n ≥ 1, the
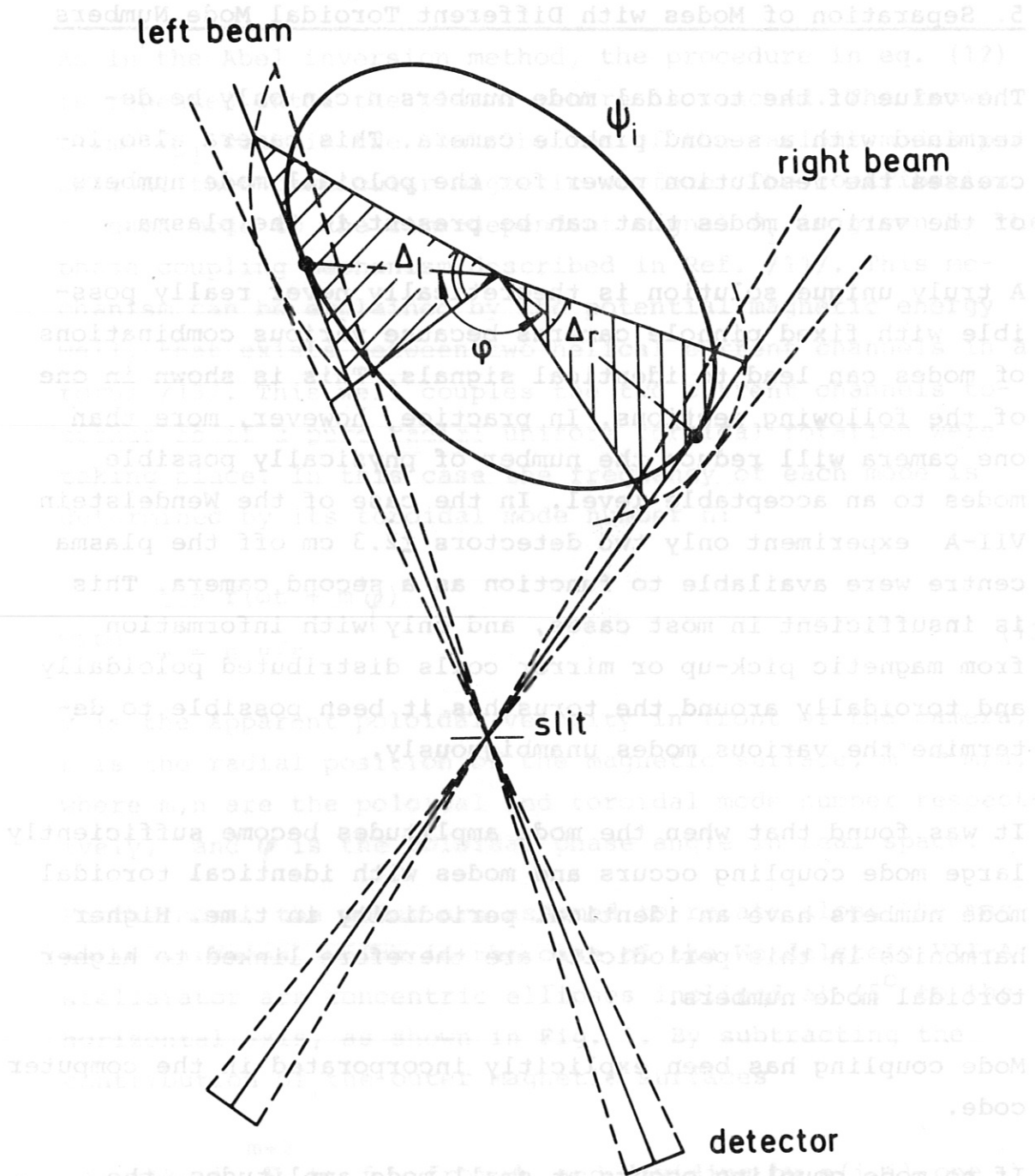
Fig. 6

choice of two periods in T all values n ≥ 2, etc.

This choice has to be consistent with other signals, e.g.
Mirnov coil signals, or it could be done automatically if
a second camera were placed at another toroidal location.

By shifting the signals over half a period T and adding
or subtracting these from the unshifted signals the
odd and even toroidal mode numbers can be separated:

$$f_{\substack{O \\ E}}(\omega t) = \frac{1}{2} \, f(\omega t) \mp f(\omega t + \P) \qquad (14)$$

$f(\omega t)$ is the signal in time,

$$0 \leq \omega t \leq 2\P.$$

$f(\omega t)$ can be writtten as a sum of its Fourier components;
it then follows that $f_O(\omega t)$ will contain the toroidal n=1
and higher <u>odd</u> components and $f_E(\omega t)$ the toroidal n=2 and
higher <u>even</u> components. In this way the two most important
toroidal mode numbers (n=1 and n=2) are separated.

<u>6. Separation of Modes with Different Poloidal Mode Numbers</u>

We shall restrict ourselves to a calculation for one camera
only. This allows only two modes to be present at the same
magnetic surface Ψ_i. The contributions of the various
poloidal modes m_1 and m_2 to the right and left-hand signals
or lines of sight f_r and f_l (see Fig. 6), respectively, can
be expressed as follows:

$$f_r = f_{m_1} \cdot \frac{\sin m_1 \Delta_r}{m_1 \Delta_r} + f_{m_2} \frac{\sin m_2 \Delta_r}{m_2 \Delta_r},$$

$$f_1 = f_{m_1}(-m_1{}^+\varphi) \cdot \frac{\sin m_1 \Delta_1}{m_1 \Delta_1} + f_{m_2}(-m_2{}^+\varphi) \cdot \frac{\sin m_2 \Delta_1}{m_2 \Delta_1}, \qquad (15)$$

where for convenience $f_m(\omega t - m^+\varphi)$ is written as $f_m(-m^+\varphi)$: the "time" ωt is omitted. See also eq. (13).

The $\frac{\sin m\Delta_r}{m \Delta_r}$ correction factors ($m = m_1$, m_2; $r = r,1$) are caused by the integration along the poloidal angle due to the finite angle resolution (Δ_r and Δ_1). Δ_r and Δ_1 increase towards the plasma centre for a fixed spatial resolution (width of the fan beam). $\Delta_{r,1}$ are the same for circular plasmas, but are different for elliptically shaped plasmas. The $\frac{\sin m\Delta_r}{m \Delta_r}$ correction factors are only approximative because it is assumed that

$$\frac{2\Delta_r \int f_m \, d}{2 \quad r} \sim f_m \cdot \int \frac{\sin m\theta \, d\theta}{2\Delta_r \quad 2 \Delta_r} = f_m \cdot \frac{\sin m\Delta_r}{m \Delta_r} \cdot \qquad (16)$$

In other words, the higher harmonics of f_m in the poloidal plane are neglected in the calculation of the correction. The division of the angle integral by $2 \Delta_r$ is due to the normalization to an ideal line of sight. It is clear that if high m-numbers are present the f_m beams must become progressively more narrow towards the plasma centre in order to resolve those higher m-number modes correctly. With the present Wendelstein VII-A pinhole camera, the $\frac{\sin m \Delta_r}{m \Delta_r}$ correction factors are everywhere close to unity for the m=1 and m=2 modes. However, an m=3 mode would encounter phase reversal and appreciable attenuation at $r \leq 1.5$ cm owing to the integration in the poloidal plane.

The following solution of eq. (15) is obtained:

$$f_{m_{1,2}} = \frac{4}{2+\alpha+\frac{1}{\alpha}} \; [h_{m_{1,2}} + \frac{1}{4}(\alpha(f_{m_{1,2}}((m_1{}^+ - m_2{}^+)\varphi) + f_{m_{1,2}}) +$$

$$\frac{1}{\alpha}(f_{m_{1,2}} + f_{m_{1,2}}((m_2{}^+ - m_1{}^+)\varphi))], \tag{17}$$

with

$$\alpha = \frac{\sin m_1 \Delta_r}{\sin m_1 \Delta_l} \cdot \frac{\sin m_2 \Delta_l}{\sin m_2 \Delta_r},$$

$$h_{m_1} = \frac{1}{4} \; (f_r - f_r \, ((m_1{}^+ - m_2{}^+)\varphi) \cdot \alpha) \frac{m_1 \Delta_r}{\sin m_1 \Delta_r} +$$

$$+ (f_1(m_1{}^+\varphi) - f_1(m_2{}^+\varphi) \cdot \frac{1}{\alpha}) \frac{m_1 \Delta_l}{\sin m_1 \Delta_l},$$

$$h_{m_2} = \frac{1}{4} \; (f_r - f_r \, ((m_2{}^+ - m_1{}^+)\varphi) \cdot \frac{1}{\alpha}) \frac{m_2 \Delta_r}{\sin m_2 \Delta_r} +$$

$$+ (f_1(m_2{}^+\varphi) - f_1(m_1{}^+\varphi) \cdot \alpha) \frac{m_2 \Delta_l}{\sin m_2 \Delta_l}.$$

The last terms of eq. (17) are usually small, so that $f_{m1,2}$ can be obtained by iteration. The convergence of the iteration exists only if $(m_1{}^+ - m_2{}^+) \neq \pm 2$ K, with K = 1,2 ... . This means that with one camera and $\varphi \sim \P$ even and odd modes can be separated but not, for instance, the m=1 and m=3 modes.

Despite the fact that $\varphi \neq \P$ one cannot distinguish between the odd modes. It is always possible to find various pairs of odd and even modes that lead to identical signals f_r and f_1. This can be seen from the following example.
An m=1 and m=2, n=1 mode combination for an ideal spatial

resolution leads to the following signals:

$$f_r = f_1 + f_2,$$

$$f_1 = f_1(-\varphi) + f_2(-2\varphi).$$

<div align="right">(18)</div>

It can readily be verified that an m=3 and m=2, n=1 mode combination leads to identical f_r and f_1 signals for

$$g_3 = -f_1(\varphi),$$
$$g_2 = f_2 + f_1 + f_1(\varphi)$$

with
$$f_r = g_2 + g_3,$$
$$f_1 = g_2(-2\varphi) + g_3(-3\varphi).$$

A second pinhole camera would solve this dilemma for the lower m-mode numbers. The problem remains, however, present for much higher m-mode numbers (m ~ 8). Usually, these mode numbers can be excluded for physical reasons, e.g. the radial profile of the safety factor q(r) or stability considerations.

Physical arguments or Mirnov coil interpretations have to be used to decide what odd and even modes are allowed in the tomographic inversion for the one pinhole camera that is used.

7. Results of Stripping Reconstruction

Three examples of reconstruction of mode structures will be given. The first example will be that of a sawtooth discharge (shot 19400) due to an m=1, n=1 tearing mode. The second example treats the case of a major current disruption due to an m=2, n=1 tearing mode. The third and last example treats the structure of an m=3, n=2 mode.

Fig. 7

SHOT:19400 2   MICRON BE.

IPP3- SME 423-83
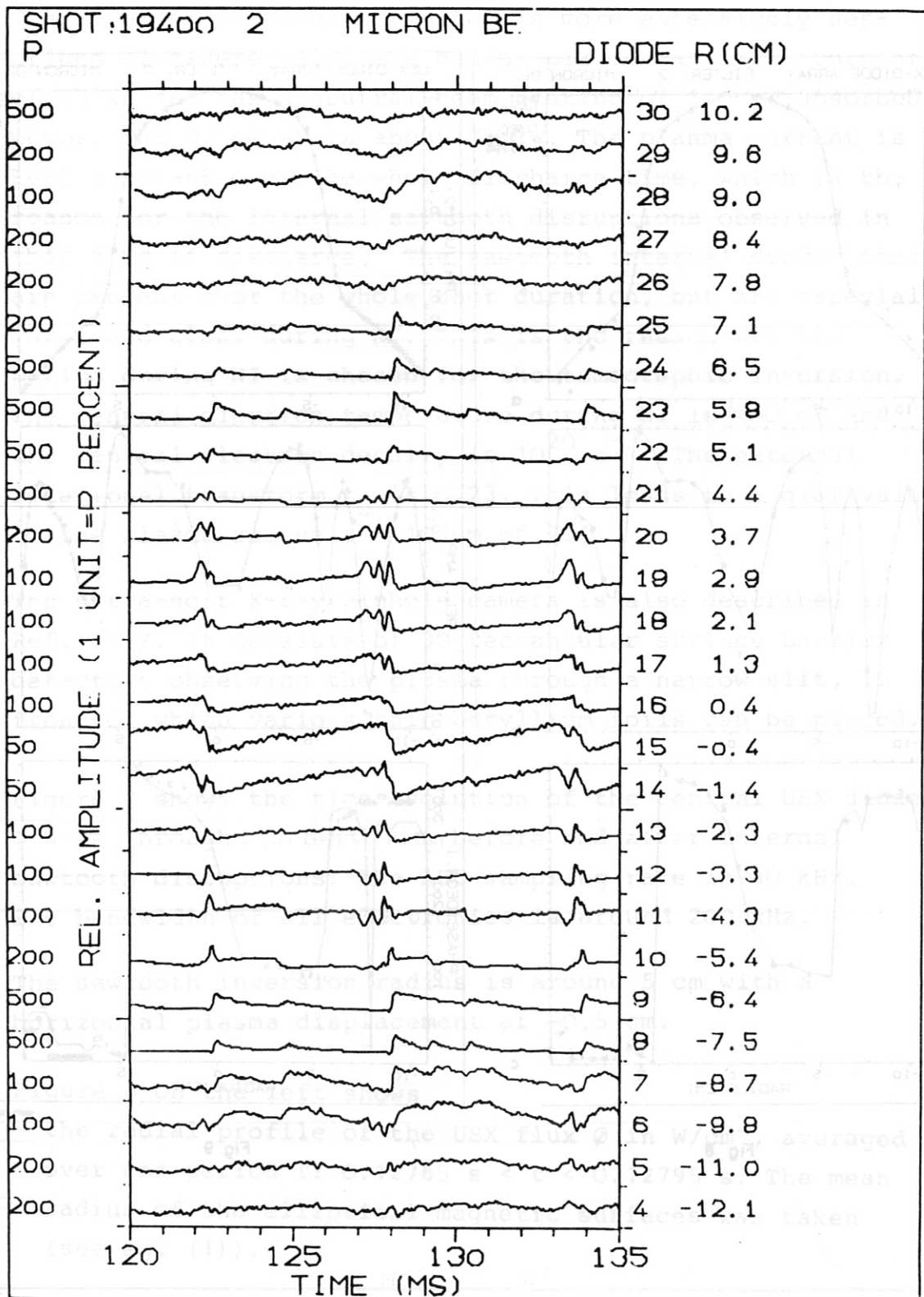
Fig. 8

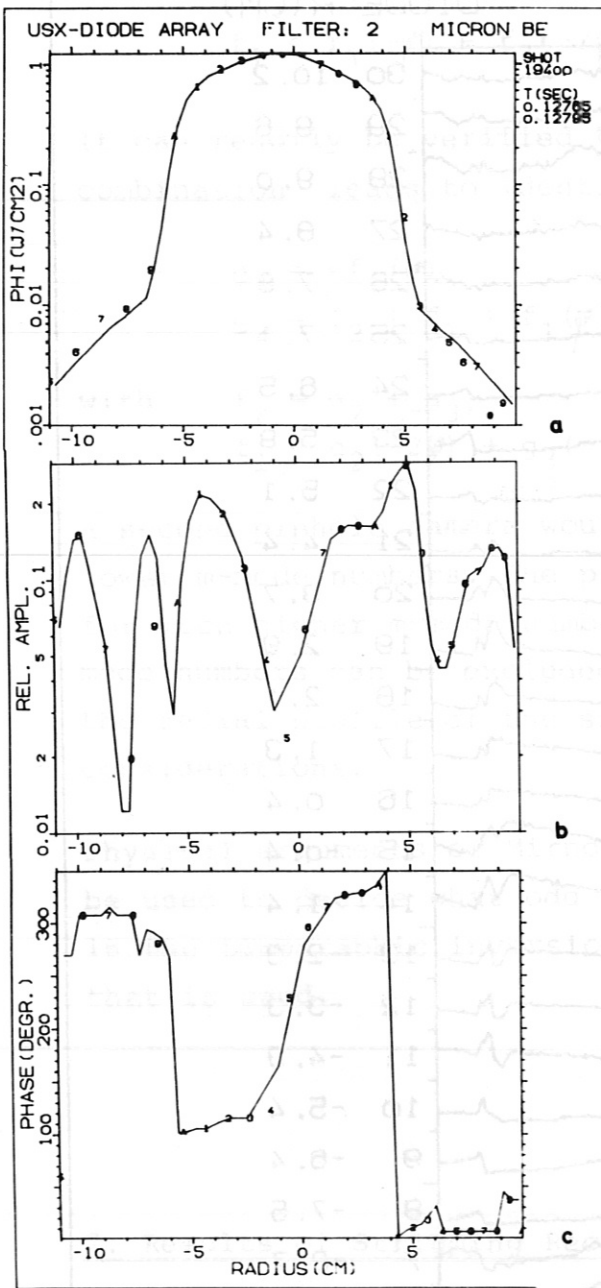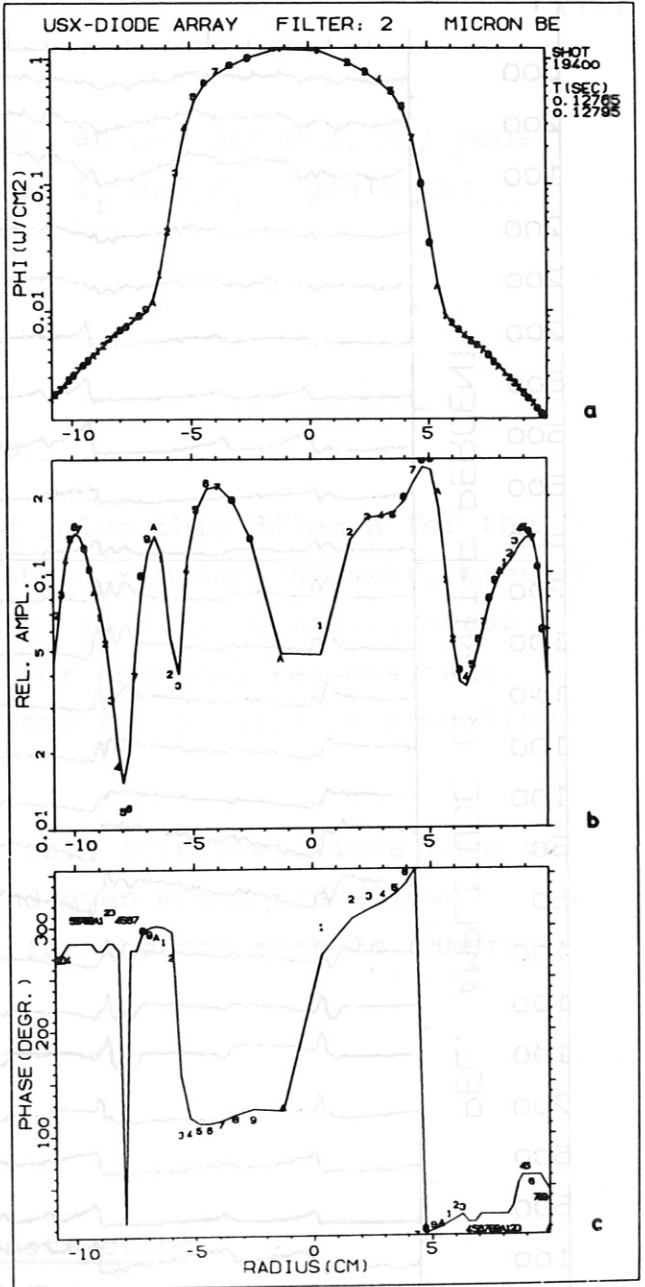**Fig. 9**

7.1 The m=1, n=1 tearing mode

The type of discharge presented is more extensively des-
cribed elsewhere /11/. The helium plasma carries a current
of 20 kA and has a neutral beam heating of 150 kW absorbed
power. The OH power is about 75 kW. The plasma current is
kept constant over the whole discharge time, which is the
reason for the internal sawtooth disruptions observed in
this kind of discharge. The sawtooth internal disruptions
are present over the whole shot duration, but are especially
large and clear during NI. This is the reason why the
period during NI is chosen for the tomographic inversion.
The central electron temperature during NI is 400 eV and
the central electron density is 10^{20} m^{-3}. The external
rotational transform t_o is 0.23. This leads to a q(a) value
at the plasma radius a = 10 cm of 2.1.

The ultra-soft X-ray pinhole camera is also described in
Ref. /11/. It consists of 30 rectangular surface barrier
detectors observing the plasma through a narrow slit, in
front of which various thin beryllium foils can be placed.

Figure 7 shows the time evolution of the central USX diode
fluxes through 2 μm beryllium before and after internal
sawtooth disruptions. The ADC-sampling rate is 40 kHz.
The bandwidth of all electronics is around 200 kHz.

The sawtooth inversion radius is around 5 cm with a
horizontal plasma displacement of -0.5 cm.

Figure 8 on the left shows
- the radial profile of the USX flux Ø in W/cm^2, averaged
  over one period T: 0.12765 s < t < 0.12795 s. The mean
  radius of the elliptical magnetic surfaces was taken
  (see eq. (1)).

- the radial profile of the relative effective amplitude A
  of the oscillations of the USX flux:

$$A = \frac{\int_T |\emptyset - <\emptyset>| dt}{\emptyset} \quad \text{with}$$

$$<\emptyset> = \int_T \emptyset \, dt$$

- the radial profile of the phase of the above oscillations
  with respect to t = 0.12765 s.
  The discrete points (marked with hexadecimal numbers
  from 1 to A) represent the real diodes. In this case
  the diodes 3 to 30 are shown. The solid lines represent
  the interpolated values (second-order interpolation
  scheme) of the virtual diodes that enter the tomographic
  inversion code.

The virtual diodes are equidistant in $\Psi \doteq r^2$, with r being
the average radius of the elliptic magnetic surfaces. This
implies that more grid points are obtained at the steep
gradients and fewer in the plasma centre. In this way
the difficulty with the high m-number modes due to the limi-
ted spatial resolution is strongly reduced.

There are about 50 % more virtual diodes than real diodes.
This allows the results of the inversion to be smoothed
without destroying any real information. In this way the
grid oscillations that appear after the inversion are elim-
inated.

Figure 9 on the right shows the radial profiles of the aver-
age flux, of the relative amplitude and of the phase of the
oscillating USX signals. The discrete points are the virtual
diode signals and the continuous lines correspond to the
recalculated signals. The recalculation is identical to a
simulation of the X-ray signals.

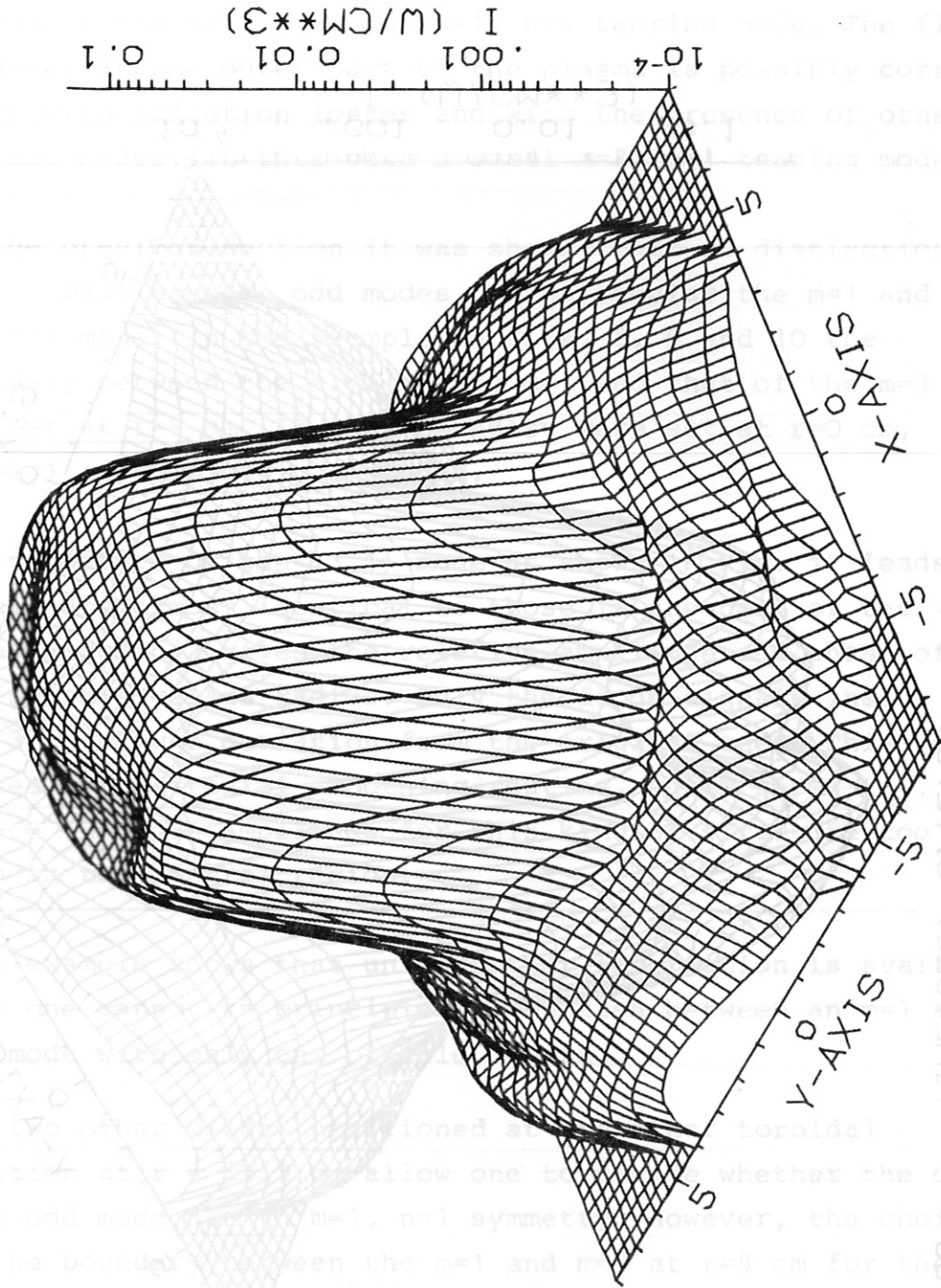ALFA 320   USX-TOMOGRAPHY
BETA 3o   TIME(SEC) 0.1278o

I (W/CM**3)

X-AXIS

Y-AXIS

SHOT 19400

Fig. 10

IPP3-SME 424-83

2   MICRON BE

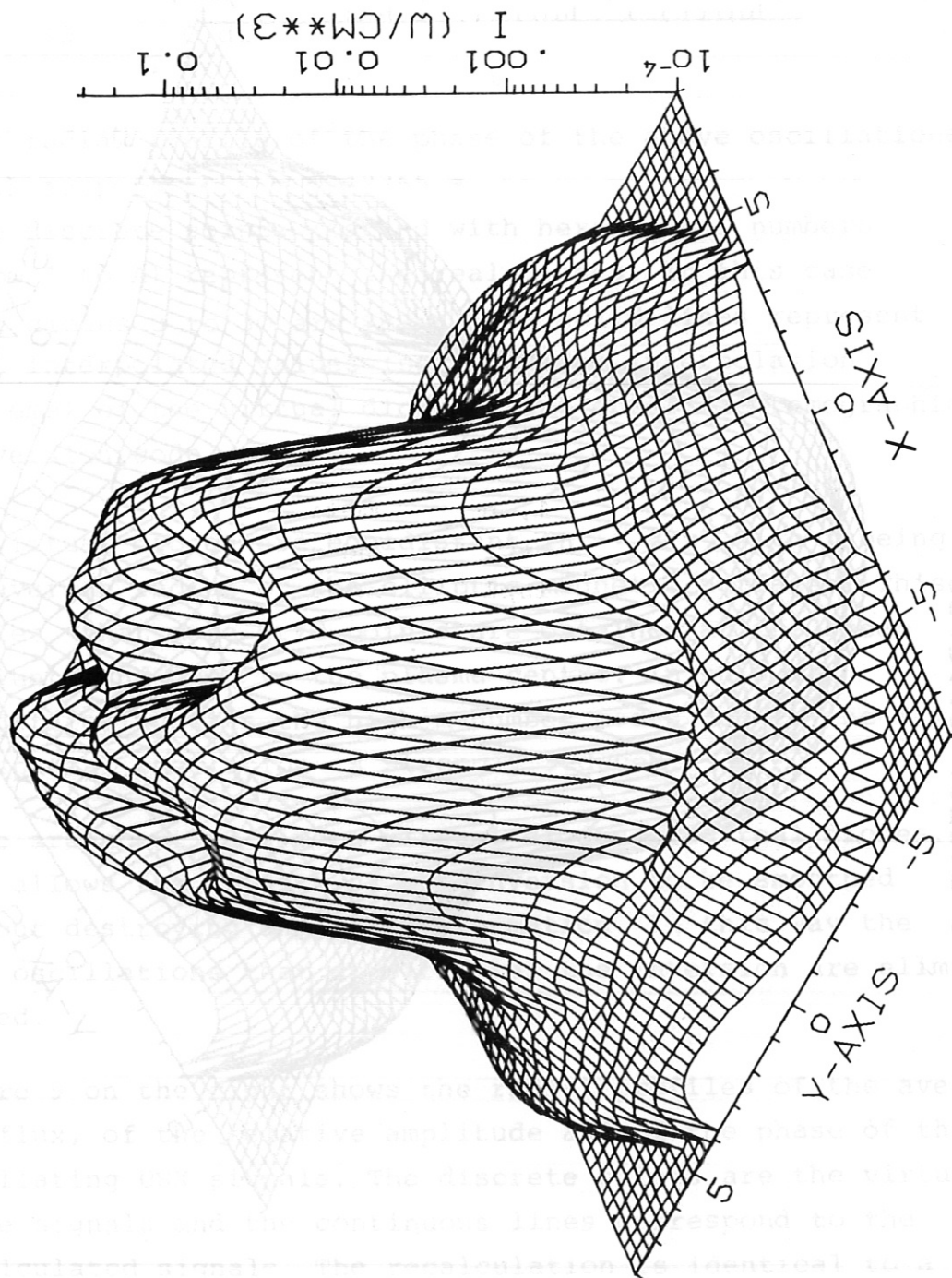ALFA 320 1st USX-TOMOGRAPHY
BETA 30 TIME(SEC) 0.12780

SHOT 19400

Fig. 11

IPP3- SME 425-83

2 MICRON BE

Figure 10 shows the USX emission structure in W/cm^3 that corresponds to the signals of Figs. 8 and 9, as a function of the poloidal angle and of the mean radius of the elliptical magnetic surfaces. The flat region near the plasma centre is due to the m=1, n=1 tearing mode. The flat shoulder at the outer part of the plasma is possibly corre- lated with radiation losses and with the presence of other tearing modes, in this case a small m=2, n=1 tearing mode.

In the previous section it was shown, that no distinction can be made between odd modes, in particular the m=1 and the m=3 mode. In the example in Figs. 8, 9 and 10 the boundary between the area of the m=1 and that of the m=3 was set at r=9 cm. If this boundary were set at r=0 cm, the m=1 is completely excluded.

The structure of the (3,1) mode as shown in Fig. 11 leads to signals almost identical to those in the case of the (1,1) mode. Figure 12 gives the relative amplitude and phase of the signals versus radius. Only the diode signals inside r < 3 cm show a deviation from the original ones. This is caused by the radial smoothing routine, which seems to reduce the mode amplitude for this kind of structure too much in the central region.

This example shows that unless other information is avail- able one cannot in principle distinguish between an m=1 and m=3 mode with only one pinhole camera.

The two other diodes positioned at the other toroidal position at r = ±2.3 cm allow one to decide whether the cen- tral odd mode has an m=1, n=1 symmetry. However, the choice of the boundary between the m=1 and m=3 at r=9 cm for the tomographic inversion displayed in Fig.10 remains arbitrary.
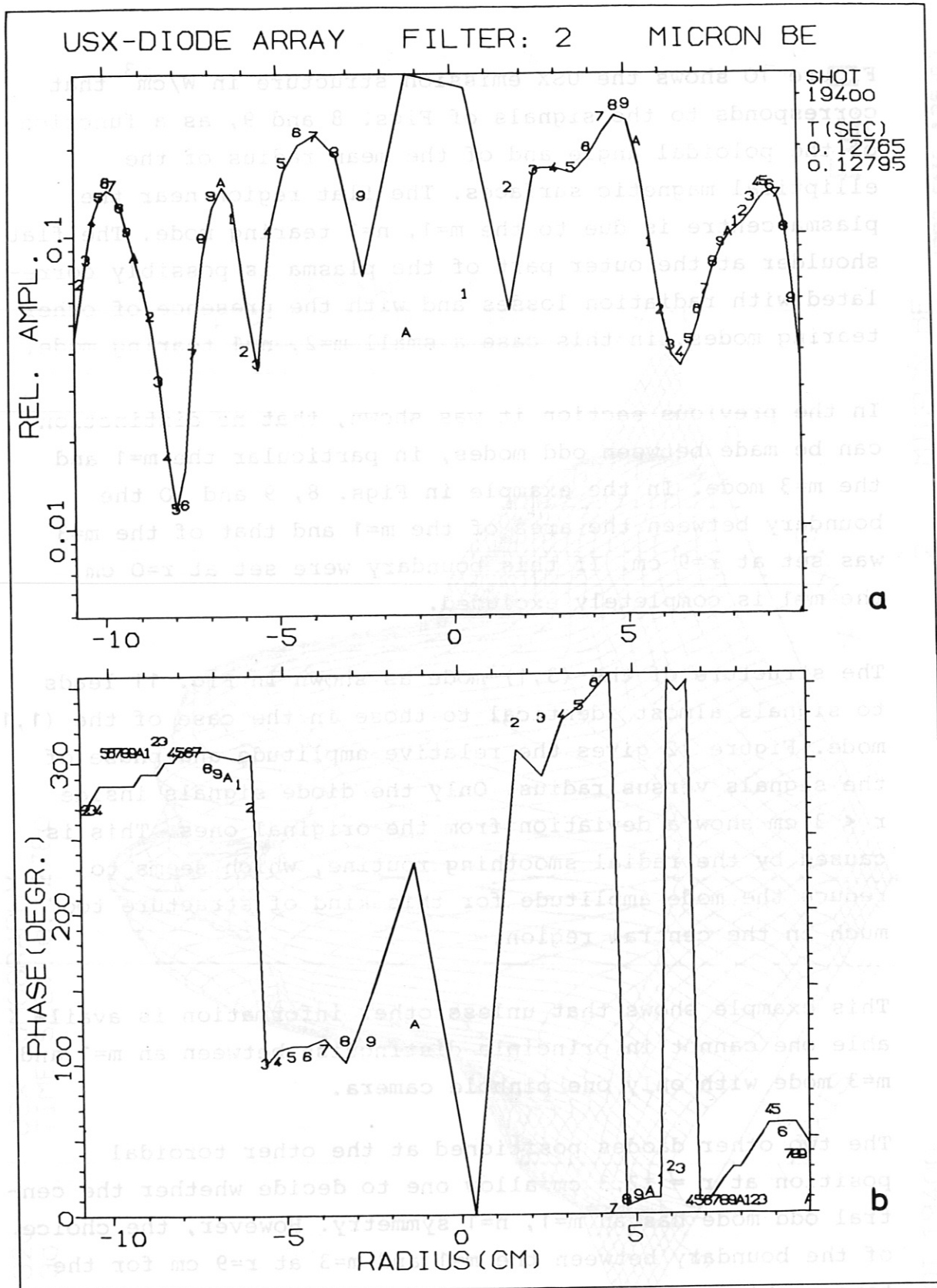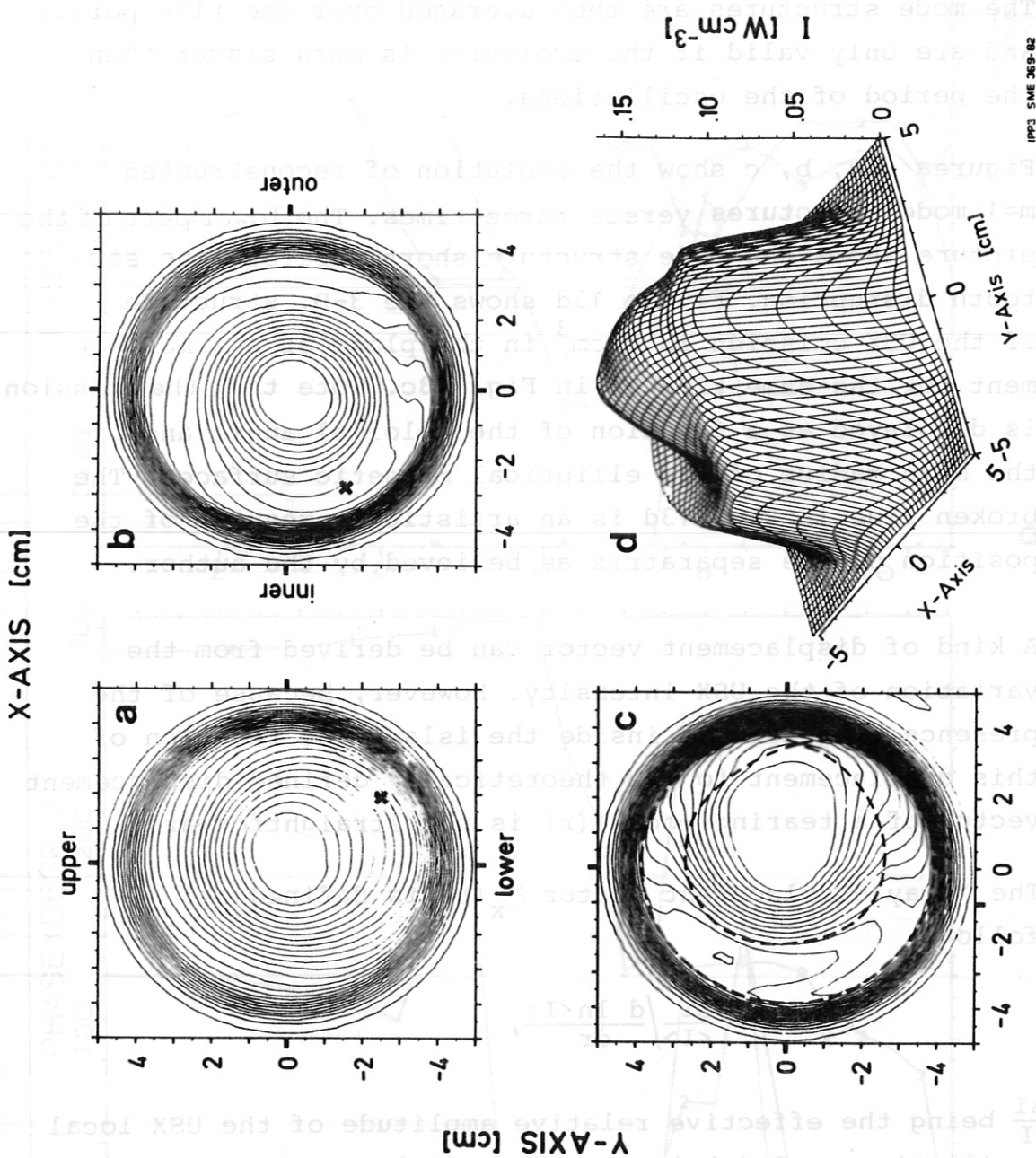
Fig. 12

- 31 -

Fig. 13

By taking various periods in time for the inversion an
evolution of the tearing mode in time can be obtained.
The mode structures are then averaged over the time period
and are only valid if the evolution is much slower than
the period of the oscillations.

Figures 13a, b, c show the evolution of reconstructed
m=1 mode structures versus three times. The lower part of the
picture shows the mode structure shortly before the saw-
tooth disruption. Figure 13d shows the 3-D. structure
of the USX emission in W/cm^3 in the plane of the measure-
ment for the same time as in Fig. 13c. Note that the emission
is displayed as a function of the poloidal angle and of
the mean radius of the elliptical magnetic surfaces. The
broken line in Fig. 13d is an artistic impression of the
position of the separatrix as believed by the author.

A kind of displacement vector can be derived from the
variation of the USX intensity. However, because of the
presence of gradients inside the island the relation of
this displacement to the theoretically defined displacement
vector of a tearing mode $\xi(r)$ is not straightforward.

The X-ray displacement vector $\xi_x(r)$ is defined as
follows:

$$\xi_x(r) = \frac{\Delta I}{<I>} \left/ \frac{d \ln <I>}{dr} \right. ,$$

$\frac{\Delta I}{I}$ being the effective relative amplitude of the USX local
oscillations. $<I>(r)$ is the USX radial intensity profile
averaged over one period. Because of the fact that effect-
ive amplitudes are used the $\xi_x(r)$, which is displayed in
the figure, has to be multiplied by about 1.5.

Figure 14 shows the X-ray displacement vector $\xi_x(r)$ and
its phase profile as a function of radius.

Fig. 14

Fig. 15

IPP3- SME 426-83
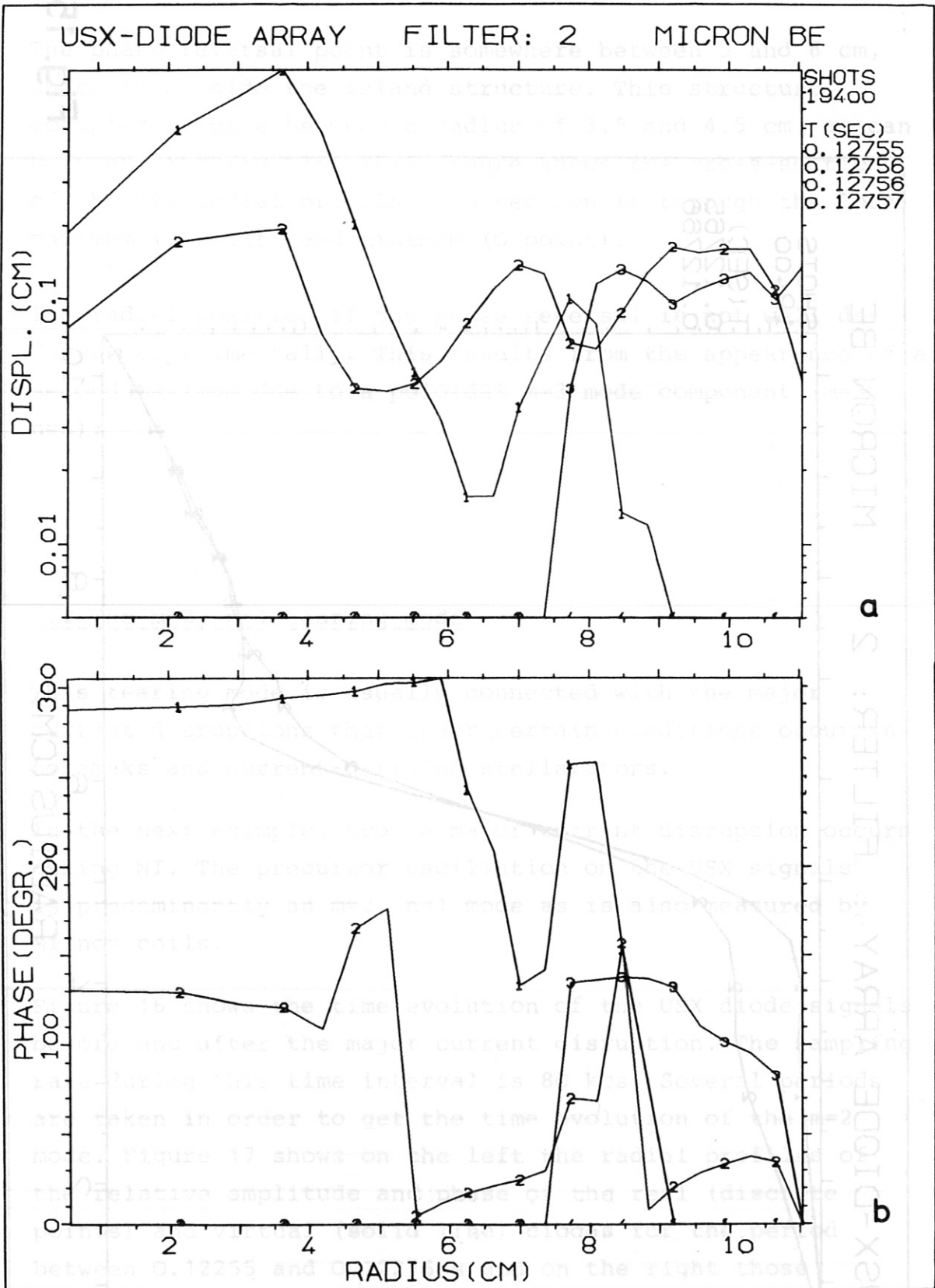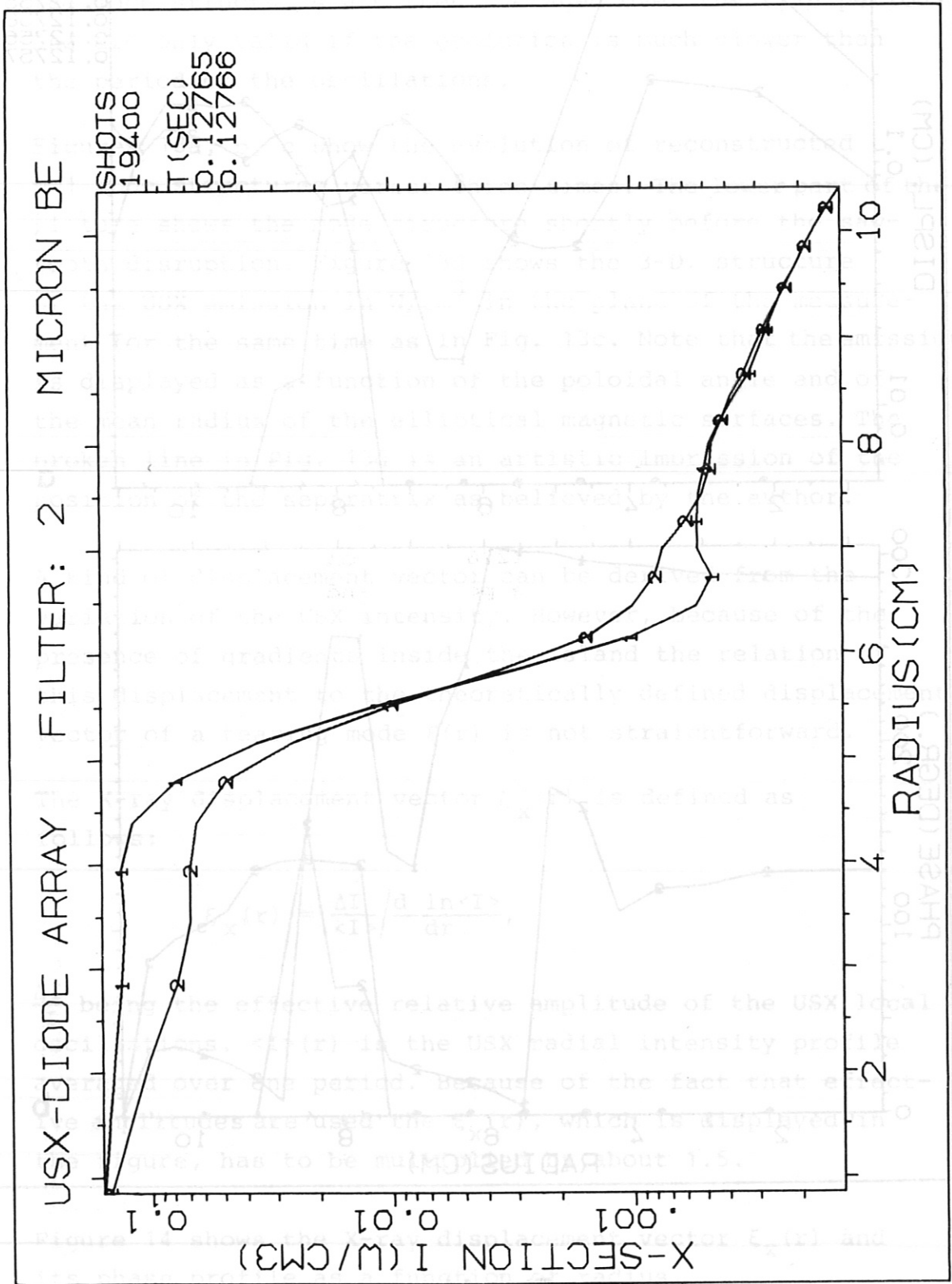
The phase reversal point is somewhere between 5 and 6 cm,
which is outside the island structure. This structure
occupies a space between a radius of 3.5 and 4.5 cm, as can
be seen from Fig. 15. This figure shows the cross-section
of the USX radial profile. The section is through the local
maximum (X point) and minimum (O point).

The radial position of the phase reversal is not well de-
fined experimentally. This results from the appearance of a
second maximum due to a poloidal m=3 mode component (m=3,
n=3).

7.2 The m=2, n=1 tearing mode

This tearing mode is usually connected with the major
current disruptions that under certain conditions occur in
tokamaks and current-carrying stellarators.

In the next example, too, a major current disruption occurs
during NI. The precursor oscillation on the USX signals
is predominantly an m=2, n=1 mode as is also measured by
Mirnov coils.

Figure 16 shows the time evolution of the USX diode signals
before and after the major current disruption. The sampling
rate during this time interval is 80 kcs. Several periods
are taken in order to get the time evolution of the m=2
mode. Figure 17 shows on the left the radial profiles of
the relative amplitude and phase of the real (discrete
points) and virtual (solid line) diodes for the period
between 0.12255 and 0.12276 s and on the right those
of the virtual (discrete points) and recalculated (solid
line) diodes.

Fig. 16

SHOT:18886 2 MICRON BE

P

DIODE R(CM)

	Amplitude	Diode	R(CM)
	500	3o	1o.2
	1000	29	9.6
	500	28	9.0
	500	27	8.4
	500	26	7.8
	500	25	7.1
	500	24	6.5
	500	23	5.8
	200	22	5.1
	500	21	4.4
	200	2o	3.7
	200	19	2.9
	200	18	2.1
	200	17	1.3
	200	16	0.4
	200	15	-0.4
	200	14	-1.4
	200	13	-2.3
	100	12	-3.3
	200	11	-4.3
	500	10	-5.4
	1000	9	-6.4
	1000	8	-7.5
	1000	7	-8.7
	500	6	-9.8
	500	5	-11.0
	500	4	-12.1
	500	3	-13.3
	500	2	-14.4
	500	1	-15.6

REL. AMPLITUDE (1 UNIT=P PERCENT)

TIME (MS)

121   122   123   124

IPP3- SME 427-83

Fig. 17

c

USX-DIODE ARRAY
FILTER :
2   MICRON BE

SHOT : 18886
TIME : 0.12274

SMOOTHING DEGR.
IN THETA : 2
IN RADIUS: 2

RAD(3,1).GT.6.0
RAD(4,2).GT.5.0

d

USX-DIODE ARRAY
FILTER :
2   MICRON BE

SHOT : 18886
TIME : 0.12274

SMOOTHING DEGR.
IN THETA : 2
IN RADIUS: 2

RAD(3,1).GT.6.0
RAD(4,2).GT.5.0

a

USX-DIODE ARRAY
FILTER :
2   MICRON BE

SHOT : 18886
TIME : 0.12212

SMOOTHING DEGR.
IN THETA : 2
IN RADIUS: 2

RAD(3,1).GT.5.0
RAD(4,2).GT.5.0

b

USX-DIODE ARRAY
FILTER :
2   MICRON BE

SHOT : 18886
TIME : 0.12254

SMOOTHING DEGR.
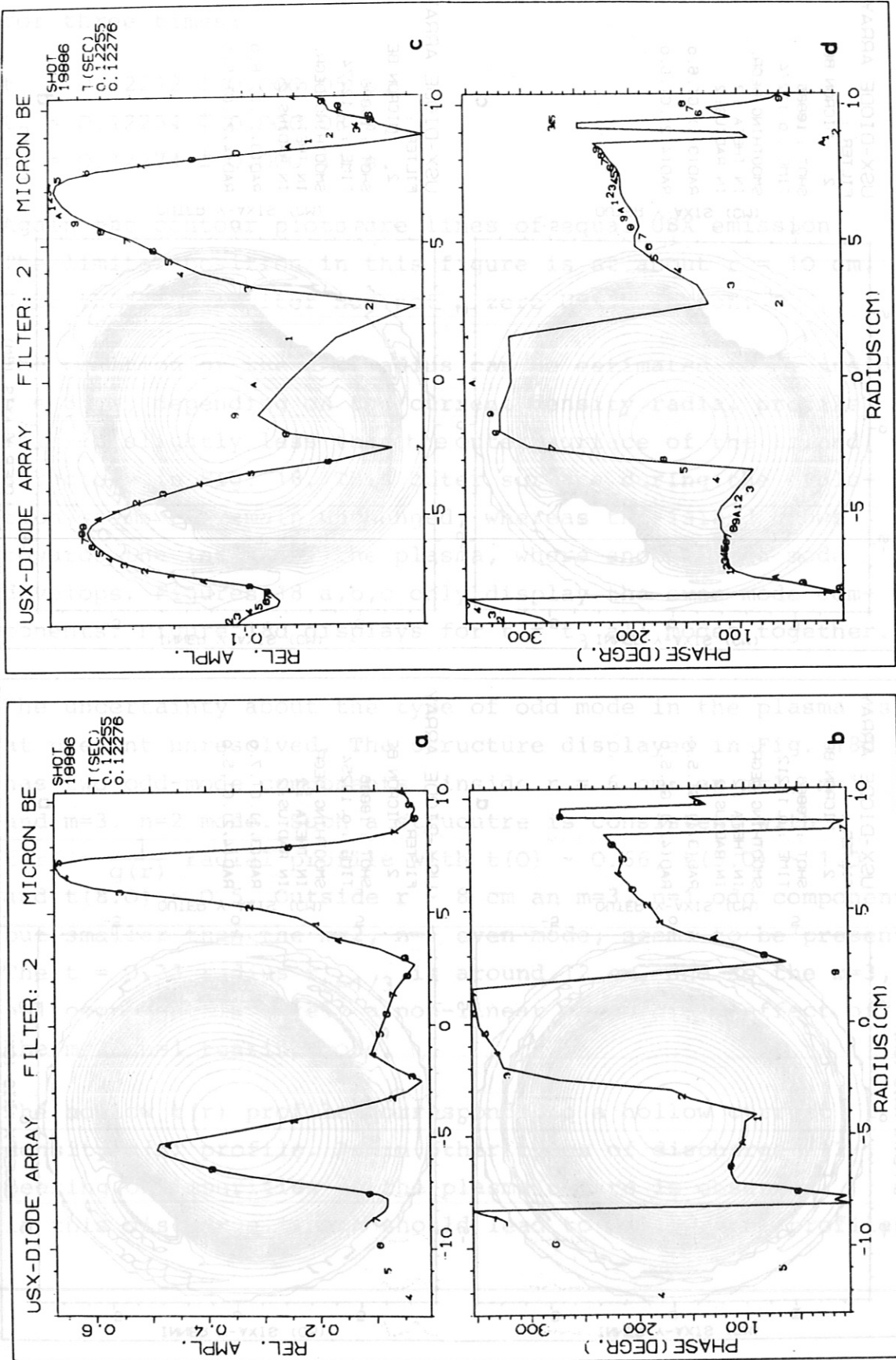IN THETA : 2
IN RADIUS: 2

RAD(3,1).GT.7.0
RAD(4,2).GT.5.0

Fig. 18

IPP3- SME 443-83
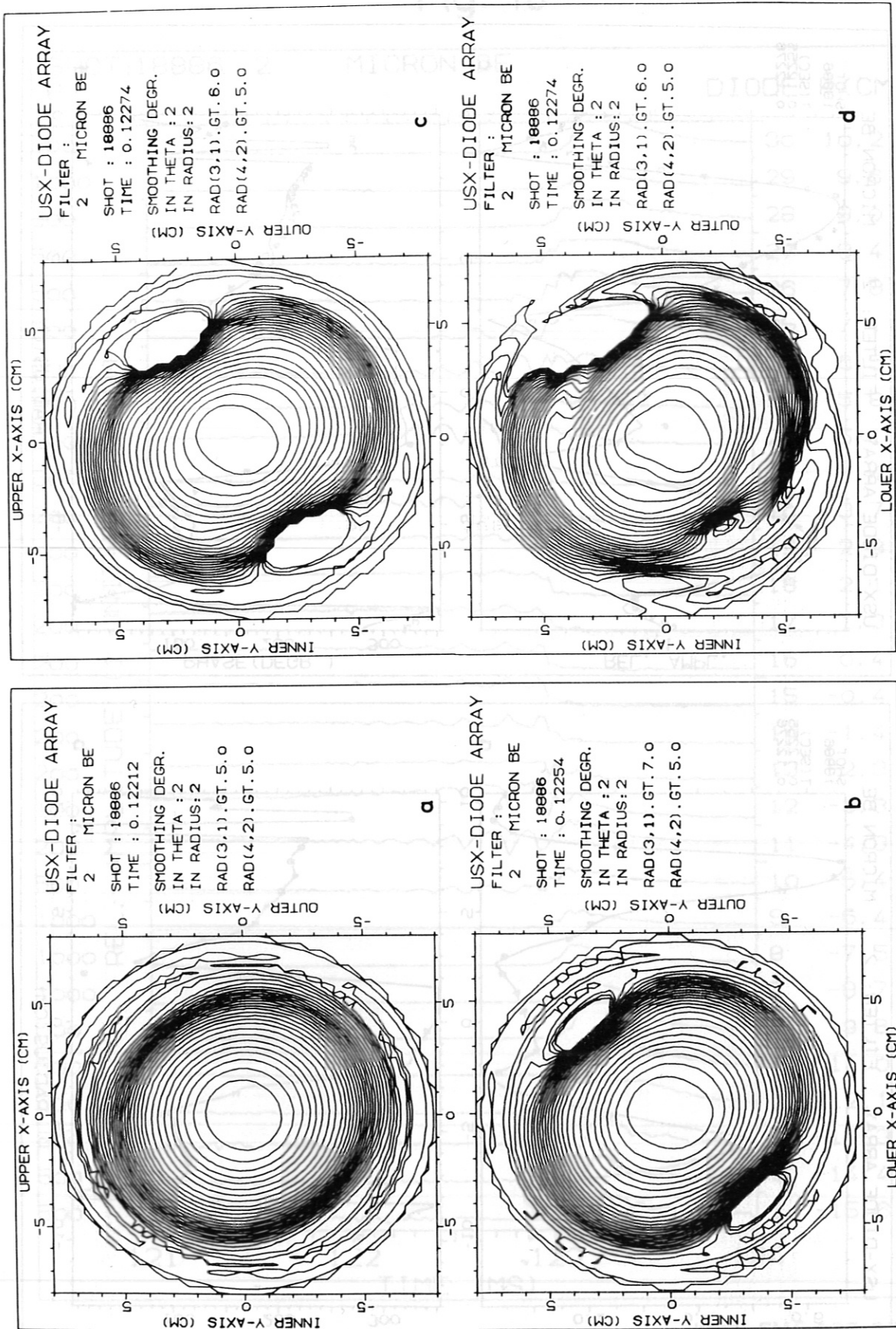
Figures 18 a,b,c show the evolution of the m=2 tearing mode
for three times:

$t_1 = 0.12212 \pm 0.000\ 05$ s,
$t_2 = 0.12254 \pm 0.000\ 08$ s,
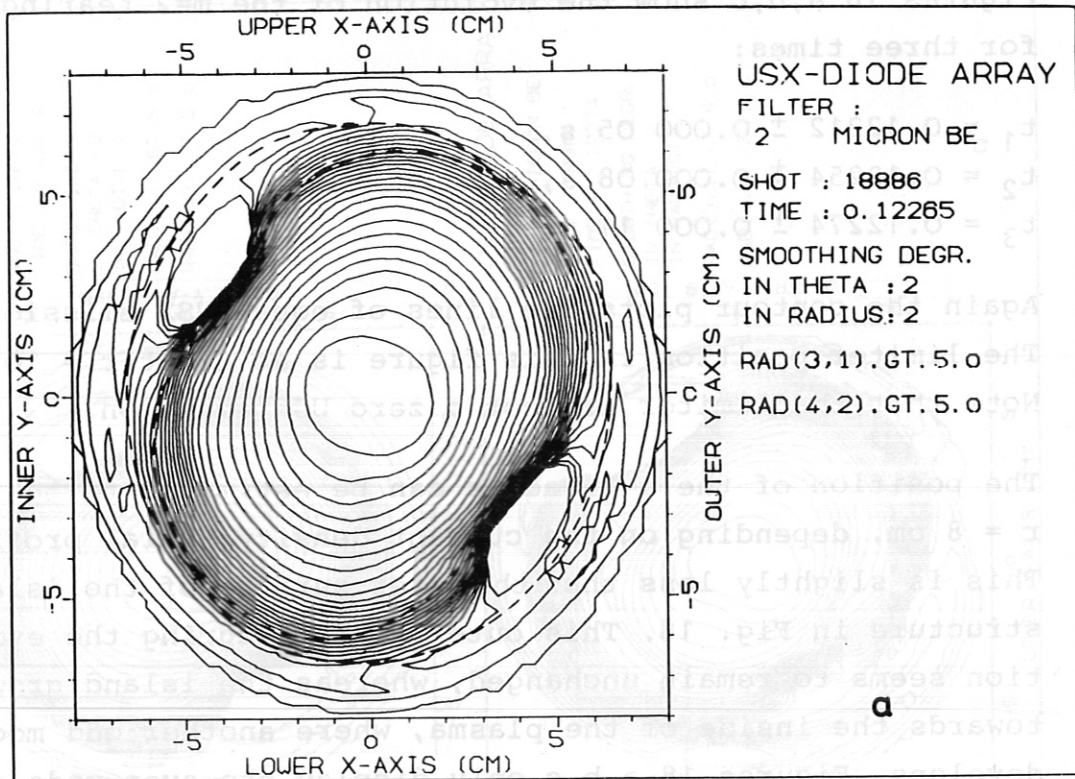$t_3 = 0.12274 \pm 0.000\ 11$ s.

Again the contour plots are lines of equal USX emission.
The limiter position in this figure is at about r = 10 cm.
Note that the limiter has not a zero USX emission.

The position of the q=2 radius can be estimated to be inside
r = 8 cm, depending on the current density radial profile.
This is slightly less than the outer surface of the island
structure in Fig. 18. This outer surface during the evolu-
tion seems to remain unchanged, whereas the island grows
towards the inside of the plasma, where another odd mode
develops. Figures 18 a,b,c only display the even-mode com-
ponents. Figure 18d displays for t = t_3 all modes together.

The uncertainty about the type of odd mode in the plasma is
at present unresolved. The structure displayed in Fig. 18d
has two odd-mode components inside r = 6 cm: an m=1, n=1
and m=3, n=2 mode. Such a strucutre is consistent with
$t(r) = \frac{1}{q(r)}$ radial profile with t(0) ~ 0.66, t(5.0) ~ 1.0
and t(8.0) ~ 0.5. Outside r ~ 8 cm an m=3, n=1 odd component,
but smaller than the m=2, n=1 even mode, seems to be present.
The t = 0.33 radius $r_{t=1/3}$ is around 12 cm, and so the m=3,
n=1 component is likely a non-linear or toroidal effect of
the m=2, n=1 tearing mode.

The hollow t(r) profile corresponds to a hollow current
density j(r) profile. As in other types of discharge /12/,
peaking of impurities in the plasma centre is observed
in this discharge, which should lead to hollow j(r) profiles.

USX-DIODE ARRAY
FILTER :
2   MICRON BE

SHOT : 18886
TIME : 0.12265

SMOOTHING DEGR.
IN THETA :2
IN RADIUS: 2

RAD(3,1).GT.5.o

RAD(4,2).GT.5.o

UPPER X-AXIS (CM)

INNER Y-AXIS (CM)

OUTER Y-AXIS (CM)

LOWER X-AXIS (CM)

a

ALFA 31o   USX-TOMOGRAPHY
BETA 6o   TIME(SEC) o.12265

i (W/CM**3)
.oo1 o.o1 o.1

Y-AXIS

X-AXIS

b

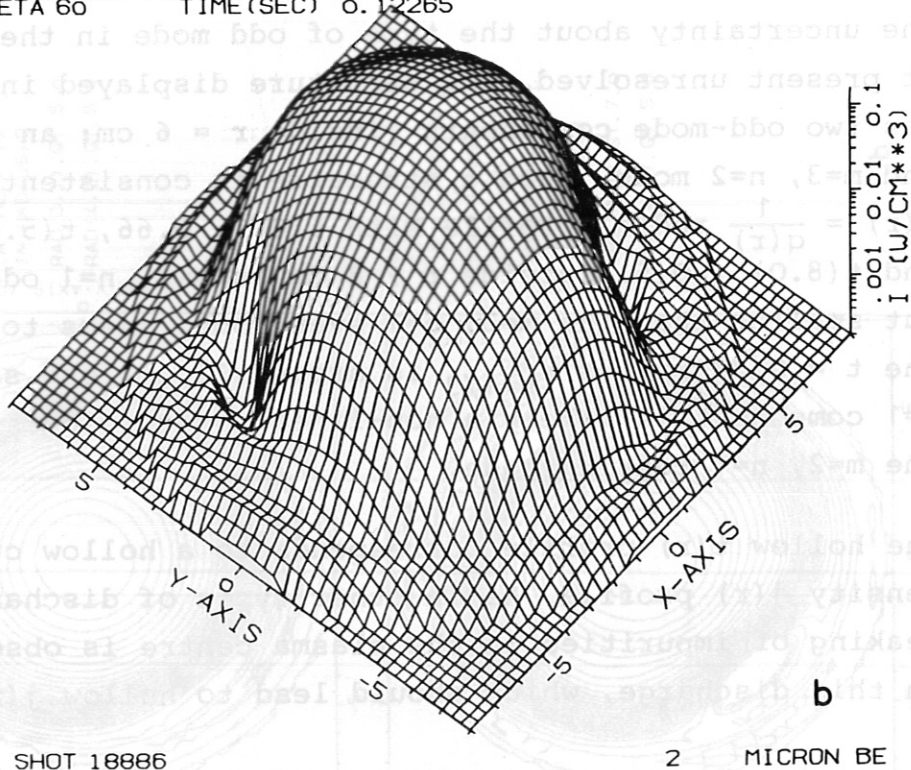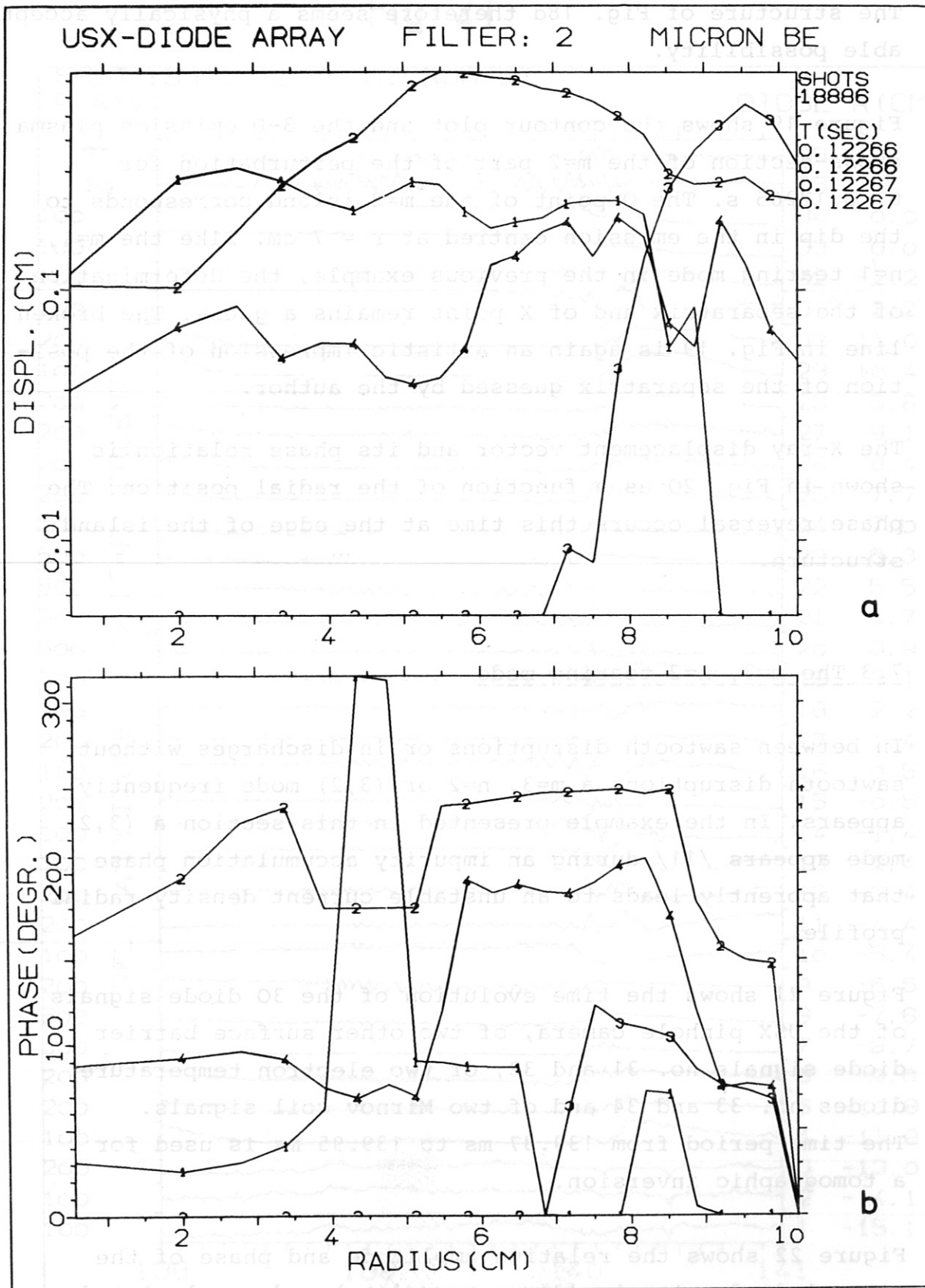SHOT 18886   2   MICRON BE

Fig. 19

Fig. 20

IPP3- SME 447-83

The structure of Fig. 18d therefore seems a physically accept-
able possibility.

Figure 19 shows the contour plot and the 3-D emission plasma
cross-section of the m=2 part of the perturbation for
t = 0.12265 s. The O point of the m=2 island corresponds to
the dip in the emission centred at r = 7 cm. Like the m=1,
n=1 tearing mode in the previous example, the determination
of the separatrix and of X point remains a guess. The broken
line in Fig. 19 is again an artistic impression of the posi-
tion of the separatrix guessed by the author.

The X-ray displacement vector and its phase relation is
shown in Fig. 20 as a function of the radial position. The
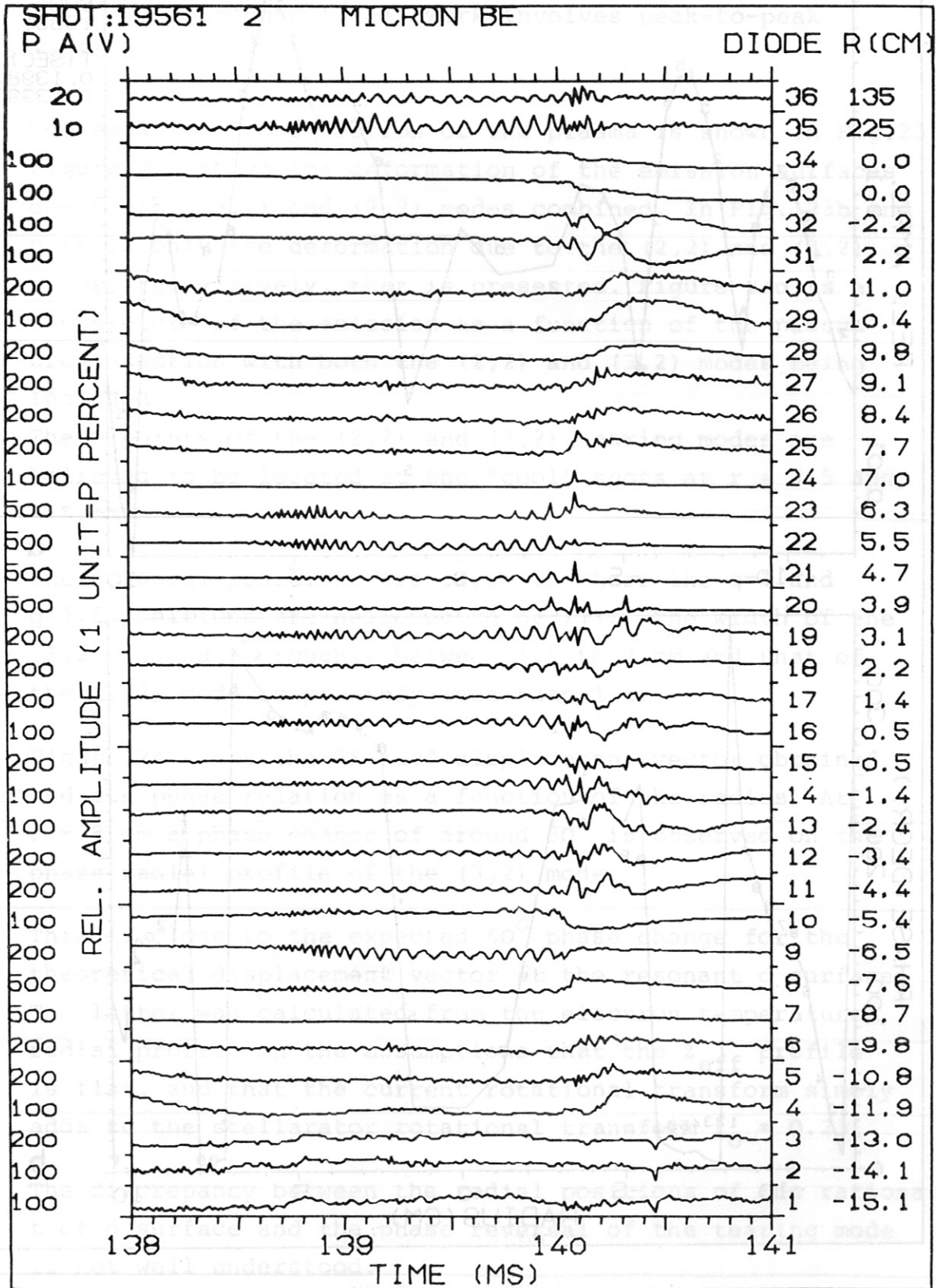phase reversal occurs this time at the edge of the island
structure.

7.3 The m=3, n=2 tearing mode

In between sawtooth disruptions or in discharges without
sawtooth disruptions a m=3, n=2 or (3,2) mode frequently
appears. In the example presented in this section a (3,2)
mode appears /11/ during an impurity accumulation phase
that apprently leads to an unstable current density radial
profile.

Figure 21 shows the time evolution of the 30 diode signals
of the USX pinhole camera, of two other surface barrier
diode signals no. 31 and 32, of two electron temperature
diodes no. 33 and 34 and of two Mirnov coil signals.
The time period from 139.87 ms to 139.95 ms is used for
a tomographic inversion.

Figure 22 shows the relative amplitude and phase of the
virtual diode signals (discrete points) and recalculated
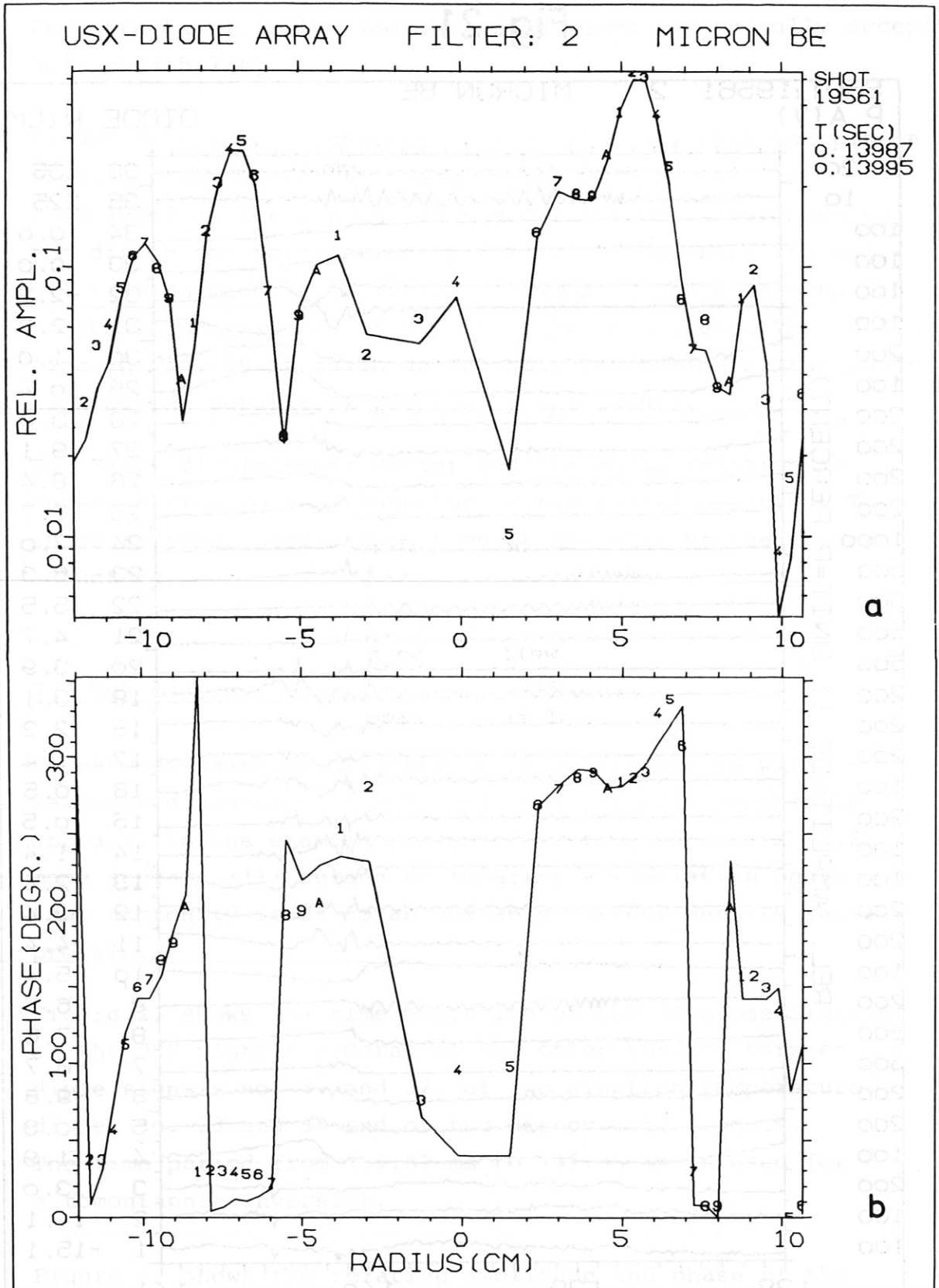signals (solid line) as a function of the mean radius.

Fig. 21

SHOT:19561 2 MICRON BE

P A(V)   DIODE R(CM)

20	36	135
10	35	225
100	34	0.0
100	33	0.0
100	32	-2.2
100	31	2.2
200	30	11.0
100	29	10.4
200	28	9.8
200	27	9.1
200	26	8.4
200	25	7.7
1000	24	7.0
500	23	6.3
500	22	5.5
500	21	4.7
500	20	3.9
200	19	3.1
200	18	2.2
200	17	1.4
100	16	0.5
200	15	-0.5
100	14	-1.4
100	13	-2.4
200	12	-3.4
200	11	-4.4
100	10	-5.4
200	9	-6.5
500	8	-7.6
500	7	-8.7
200	6	-9.8
200	5	-10.8
100	4	-11.9
200	3	-13.0
100	2	-14.1
100	1	-15.1

REL. AMPLITUDE (1 UNIT=P PERCENT)

TIME (MS)

138   139   140   141

IPP3- SME450-83

Fig. 22

It should be noted that comparison with the analysis of Ref. /11/ throughout this work involves peak-to-peak amplitudes.

The emission cross-section of the plasma is shown in Fig.23. Figure 23a shows the deformation of the emission surfaces due to the (3,2) and (2,2) modes combined. In Fig. 23b and c it is only the deformation due to the (2,2) and (3,2) modes, respectively, that is presented. Figure 23d is a 3-D picture of the emission as a function of the plasma cross-section with both the (2,2) and (3,2) modes being included.
The O points of the (2,2) and (3,2) tearing modes are believed to be located at the "cool" spots at r = 3.5 and 6.5 cm.

These radial positions are close to where the q=1 and q=1.5 positions are believed to be /11/. The width of the (3,2) island is roughly between 1.5 to 2 cm and that of the (2,2) mode is probably less than 1 cm.

Figure 24 shows the "X-ray" displacement vector obtained and its phase relation as a function of the radius. At r = 8 cm a phase change of around 50° is observed on the phase radial profile of the (3,2) mode.

This is close to the expected 60° phase change for the theoretical displacement vector at the resonant q surface. The latter was calculated from the electron temperature radial profile on the assumptions that the Z_{eff} profile is flat, and that the current rotational transform simply adds to the stellarator rotational transform $t_o = 0.23$.

The discrepancy between the radial positions of the rational t or q-surface and the phase reversal of the tearing mode is not well understood.
A possible cause might well be the heat transport over the X point, extending the hot region further outwards than the actual shift of the surfaces.
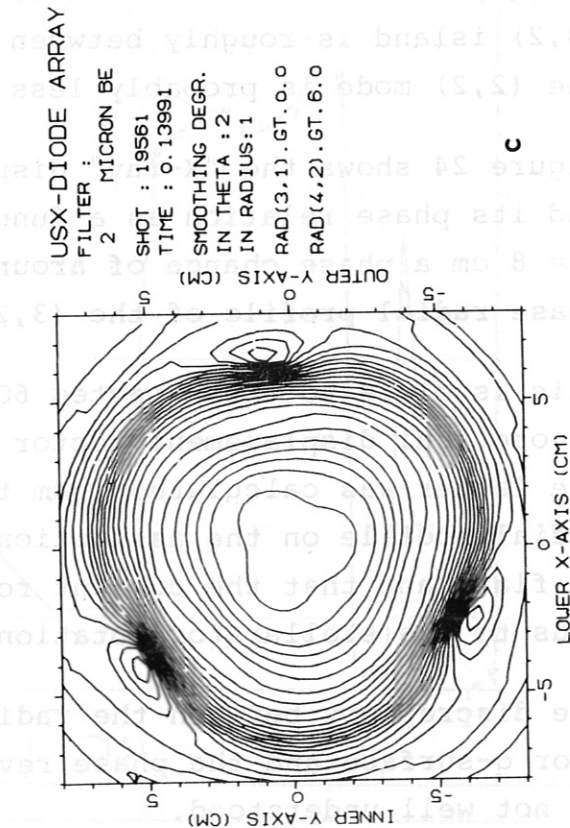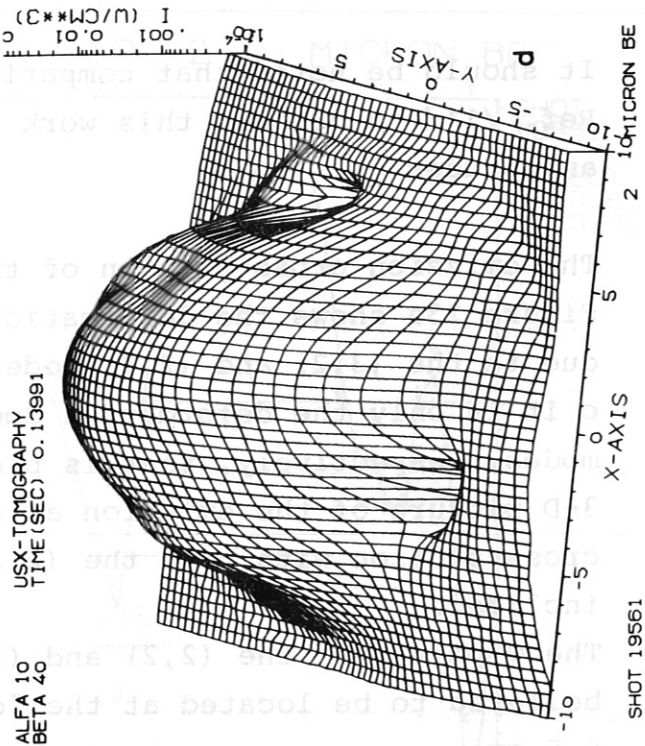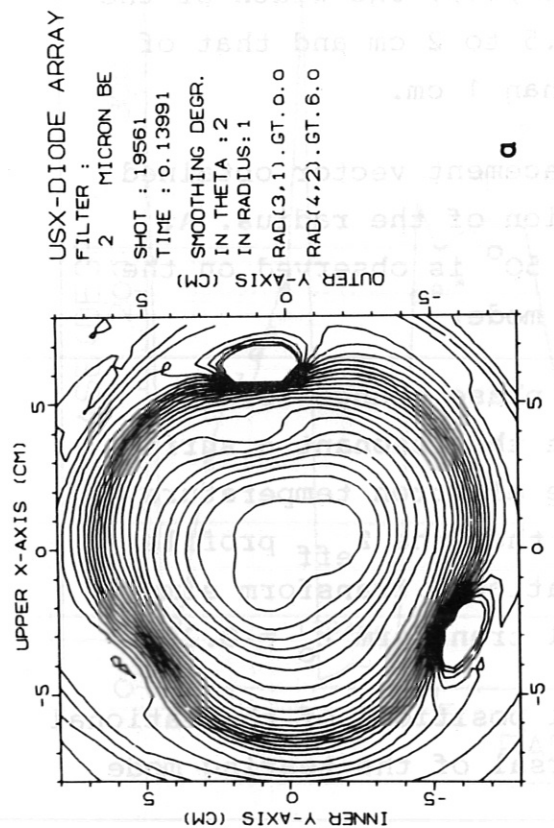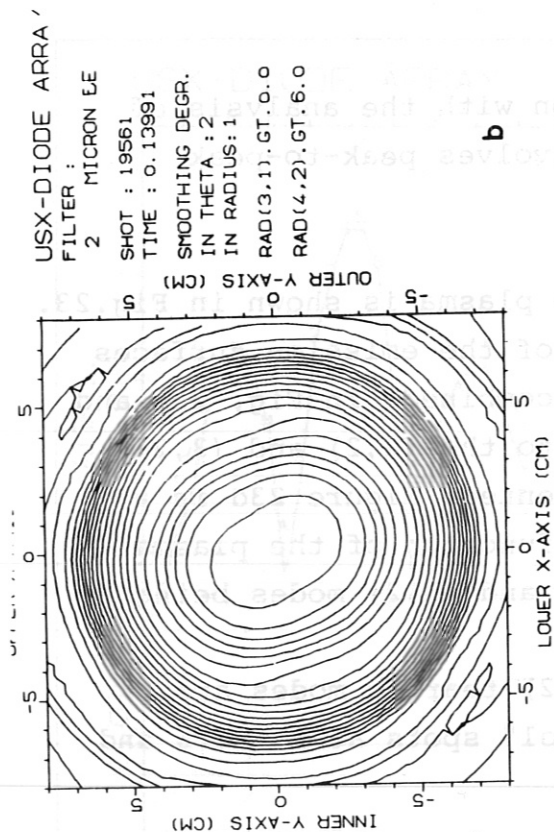
Fig. 23

USX-DIODE ARRA'
FILTER :
2 MICRON EE

SHOT : 19561
TIME : 0.13991

SMOOTHING DEGR.
IN THETA : 2
IN RADIUS: 1
RAD(3.1).GT.0.0
RAD(4.2).GT.6.0

b

USX-TOMOGRAPHY
TIME(SEC) 0.13991

ALFA 10
BETA 40

USX-DIODE ARRAY
FILTER :
2 MICRON BE

SHOT : 19561
TIME : 0.13991

SMOOTHING DEGR.
IN THETA : 2
IN RADIUS: 1
RAD(3.1).GT.0.0
RAD(4.2).GT.6.0

a

USX-DIODE ARRAY
FILTER :
2 MICRON BE

SHOT : 19561
TIME : 0.13991

SMOOTHING DEGR.
IN THETA : 2
IN RADIUS: 1
RAD(3.1).GT.0.0
RAD(4.2).GT.6.0

c

d

SHOT 19561

IPP3-SME 441-83

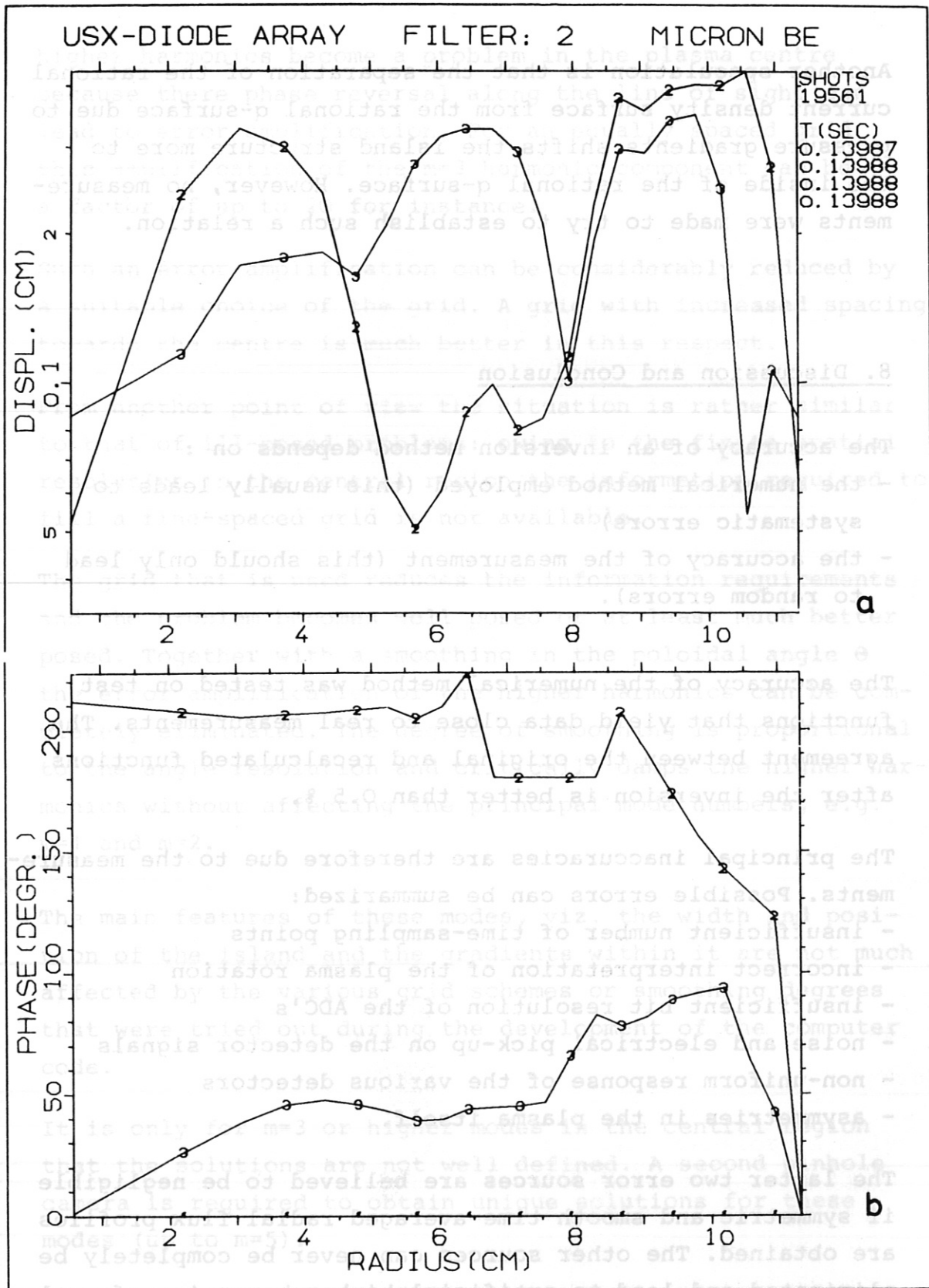Fig. 24

Another speculation is that the separation of the rational current density surface from the rational q-surface due to pressure gradients shifts the island structure more to the inside of the rational q-surface. However, no measurements were made to try to establish such a relation.

8. Discussion and Conclusion

The accuracy of an inversion method depends on :
- the numerical method employed (this usually leads to systematic errors)
- the accuracy of the measurement (this should only lead to random errors).

The accuracy of the numerical method was tested on test functions that yield data close to real measurements. The agreement between the original and recalculated functions after the inversion is better than 0.5 %.

The principal inaccuracies are therefore due to the measurements. Possible errors can be summarized:
- insufficient number of time-sampling points
- incorrect interpretation of the plasma rotation
- insufficient bit resolution of the ADC's
- noise and electrical pick-up on the detector signals
- non-uniform response of the various detectors
- asymmetries in the plasma itself.

The latter two error sources are believed to be negligible if symmetric and smooth time-averaged radial flux profiles are obtained. The other sources can never be completely be eliminated and lead to artificial higher harmonics of real mode structures. In the inversions presented here these

higher harmonics become a problem in the plasma centre
because there phase reversal along the line of sight can
lead to error amplification. For an equally spaced grid
this amplification of the $m=3$ harmonic component can be
a factor of up to 20 for instance.

Such an error amplification can be considerably reduced by
a suitable choice of the grid. A grid with increased spacing
towards the centre is much better in this respect.

From another point of view the situation is rather similar
to that of ill-posed problems: owing to the finite spatial
resolution in the central region the information required to
fill a fine-spaced grid is not available.

The grid that is used reduces the information requirements
and the problem becomes well posed or at least much better
posed. Together with a smoothing in the poloidal angle θ
the error amplification of the higher harmonics can be com-
pletely eliminated. The degree of smoothing is proportional
to the angle resolution and critically damps the higher har-
monics without affecting the principal mode numbers, e.g.
$m=1$ and $m=2$.

The main features of these modes, viz. the width and posi-
tion of the island and the gradients within it are not much
affected by the various grid schemes or smoothing degrees
that were tried out during the development of the computer
code.

It is only for $m=3$ or higher modes in the central region
that the solutions are not well defined. A second pinhole
camera is required to obtain unique solutions for these
modes (up to $m=5$).

Acknowledgements

References

/1/ G.T. Herman (editor), Image Reconstruction from Pro-
jections, Topics in Applied Physics, Vol. 32,
Springer-Verlag (1979).

/2/ R.A. Brooks, G. DiChiro, Principles of Computer Assisted
Tomography (CAT) in Radiography and Radioisotopic
Imaging, Phys. Med. Biol., 1976, Vol. 21, No. 5,
689-732.

T.F. Budinger, G.T. Gulberg, Three-Dimensioned Recon-
struction in Nuclear Medicine Emission Imaging,
IEEE Transactions on Nuclear Science, Vol. NS-21,
June 1974.

/3/ N.R. Sauthoff, S. von Goeler, Techniques for the Re-
construction of Two-Dimensional Images from Projections,
IEEE Trans. in Plasma Sci., PS-7(3), 141-147 (1979).

/4/ F. Pohl, Abel Equation for Asymmetric Emission,
Max-Planck-Institut für Plasmaphysik Rep. IPP 6/173
(1978).

/5/ Y. Schivell, Methods for Reconstructing Spatial Distri-
butions of Radiation from Plasmas, Princeton Plasma
Physics Lab. Rep. PPPL-1557 (1979).

/6/ F. Seguin, R. Chase, R. Petrasse, M. Gerassimenko,
Magnetic Island Structure in the Alcator-A Tokamak,
Bull. of the Am. Phys. Soc., Vol. 24, No. 8 (1979).

/7/ M.A. Dubois, D.A. Marty, A. Pochelon, Method of Car-
tography of q=1 Islands during Sawtooth Activity in
Tokamaks, Nuclear Fusion, Vol. 20, 11 (1980).

/8/ A. Weller, Simulation of X-ray Signals, Max-Planck-
Institut für Plasmaphysik Report, IPP 2/251 (1980).

/9/ P. Smeulders, Second Order Abel Inversion with Allowance for the Spatial Resolution, Max-Planck-Institut für Plasmaphysik Rep. IPP 2/240 (1978) (Note: Formula (5) in this reference should be replaced by:

$$\Psi' = (1(m-1) + (d_2/_2 - S_2) (m+1))^2/(2m^2+2)).$$

/10/ R.N. Bracewell, Correction for Collimator Width (Restoration) in Reconstructive X-Ray Tomography, J. of Comp. Ass. Tomography 1(1), 1977.

/11/ W VII-A-Team, Mode and Sawtooth Behaviour during Neutral Beam Injection in the W VII-A Stellarator, Max-Planck-Institut für Plasmaphysik Rep. IPP 2/250 (1980).

/12/ W VII-A Team and NI Team, Evolution of Radiation Losses and Importance of Charge Exchange between Impurities and Injected Beam Neutrals in the W VII-A Stellarators, Abstracts of 5th General Conf. of the EPS, Istanbul (Sept. 1981).

/13/ A. Weller, private communication.